

Tuning the valence of MnO_x cathodes reveals the universality of the proton-coupled electrodisolution/electrodeposition mechanism in rechargeable aqueous Zn batteries

Arvinder Singh,^{1,2} Christel Laberty-Robert,^{2} Véronique Balland,^{1*} and Benoît Limoges^{1*}*

¹Université de Paris, Laboratoire d'Electrochimie Moléculaire, UMR CNRS 7591, F-75013 Paris, France.

²Chimie de la Matière Condensée, Sorbonne Université - CNRS, UMR 7574, 4 place Jussieu, 75005 Paris, France.

E-mails: christel.laberty@sorbonne-universite.fr; veronique.balland@u-paris.fr; limoges@u-paris.fr

Keywords: spinel Mn₃O₄, zinc battery, buffered electrolyte, charge storage mechanism

The charge storage mechanism of manganese oxides (MnO_x) in rechargeable mild aqueous Zn batteries is still a matter of debate, with no consensus on mechanism and charge carriers. In this work, we address this issue by relying on a quantitative and comparative electrochemical study of low-valence crystalline MnO_x cathodes in a range of aqueous electrolytes, with a primary focus on spinel Mn₃O₄. Our results demonstrate that the oxidation state of Mn in MnO_x structures as well as their degree of crystallinity have little impact on the electrochemical reactivity, all MnO_x being fully converted into soluble Mn²⁺ upon discharge. We further reveal that this electrodisolution mechanism is affected by Mn₃O₄ dismutation in the most acidic electrolytes. Accordingly, the true thermodynamics and kinetics of Mn₃O₄ are only accessible at mildly acidic to neutral pH values. In addition, we confirm the phase transformation of Mn₃O₄ to Mn₅O₈ upon galvanostatic oxidation, and demonstrate that this transformation only proceeds in Mn²⁺-free electrolytes, since otherwise amorphous MnO₂ electrodeposits on top of Mn₃O₄. Finally, we conclude that regardless of the starting MnO_x material, after the first discharge or a first charge/discharge cycle, subsequent charge/discharge cycles rely on a reversible proton-coupled electrodeposition of amorphous MnO₂.

1. Introduction

In recent years, rechargeable Zn/MnO₂ batteries capable to operate in near-neutral aqueous electrolytes are getting significant attention,¹⁻³ especially since the remarkable cycling performance reported by Pan *et al.*⁴ In such batteries, manganese oxides are excellent complementary cathodes due to their relatively high theoretical capacity (up to 616 mAh/g if exploiting the 2 e⁻ contained in Mn^{IV}O₂ to reach Mn^{II}), diverse valence states, non-toxicity, and abundance.⁵⁻⁷ So far, amorphous MnO₂ as well as its different crystalline phases, ranging from tunnel (*e.g.*, α-MnO₂, γ-MnO₂, β-MnO₂), layered (δ-MnO₂) and spinel (λ-MnO₂), have been investigated in aqueous Zn batteries.^{3,8,9} A high number of studies report that during the first few cycles (also called activation cycles), these MnO₂ structures transform into different phases ranging from spinel-like Mn^{III} structures (ZnMn₂O₄), to layered (or tunnel) Zn-birnessite or Zn_xMnO₂ structures, which subsequently are claimed to reversibly disinsert/insert the multivalent Zn²⁺ cations (or a combination of Zn²⁺ and H⁺ disinsertion/insertion) for the rest of the cycles.^{1-3,8-10} However, these mechanistic interpretations contradict a growing number of publications clearly demonstrating that, regardless of the crystalline structure of MnO₂, the charge storage mechanism in mild aqueous electrolytes relies on a reversible process of electrodisolution of the solid MnO₂ into soluble Mn²⁺.¹¹⁻²⁵ Some works have also demonstrated that the protons essential for this electrodisolution process are provided by the hexaaquo complexes of Zn²⁺.^{11,15,16}

Despite intrinsically smaller gravimetric capacities than MnO₂, crystalline low-valence Mn-oxide structures (MnO_x) were also proposed for the development of rechargeable mild aqueous Zn/MnO_x batteries.²⁶⁻⁴¹ Similarly as for MnO₂, it has been claimed that Zn²⁺ ions insert reversibly into these low-valence MnO_x structures. This has been notably reported for spinel Mn₃O₄ (*i.e.*, Mn^{II}Mn^{III}₂O₄)^{32,39,40} and sesquioxide α-Mn₂O₃,²⁹ as well as lower valence oxides such as Mn₂O₃ derivatives,^{26,27} and even MnO.²⁸ In contrast, Stoševski *et al.* observed no structural transformation or direct evidence of Zn²⁺ intercalation into hausmannite Mn₃O₄ structure.³⁶ Still, they report on an activation process associated with the precipitation of a zinc layered double hydroxide at the electrode surface, revealing that proton plays a significant role in the charge-storage mechanism.³⁶ Further, Sassin *et al.* demonstrated the inability of spinel ZnMn₂O₄ to release Zn²⁺ ions upon charge.⁴¹ In contrast, other studies on Mn₃O₄ suggest an initial activation mechanism leading to the irreversible transformation of Mn₃O₄ into MnO₂, this later being the active material capable of reversibly (co-)inserting Zn²⁺ and/or H⁺.^{30,34-37,42,43} For instance, Hao *et al.* have described an electrochemically induced phase transformation of spinel Mn₃O₄ into birnessite MnO₂, which thereafter is assumed to

reversibly co-insert Zn^{2+} and H^+ upon cycling.³⁰ In contrast, Wang *et al.* have concluded to an unexpected phase transition from spinel Mn_3O_4 to $\epsilon\text{-MnO}_2$, and a subsequent charge storage mechanism associated on reversible proton insertion.³¹

What finally emerges from all these studies is that the electrochemical reactivity of MnO_x electrodes in mild aqueous electrolytes is far from being well understood, with no consensus on the mechanism as well as the nature of charge carriers. The objective of the present work is to address this issue by relying on a comparative quantitative study of MnO_x crystalline structures (prepared with distinct valence states) in a Zn/MnO_x battery configuration, containing buffered or unbuffered mild aqueous electrolytes. For such a purpose, we have taken advantage of crystalline MnO_x electrodes obtained from conformal electrodeposition of a thin film of amorphous MnO_2 on the surface of free-standing 3D carbon nanofibers (CNFs). The as-deposited amorphous MnO_2 coating on CNFs (amorphous $\text{MnO}_2@\text{CNF}$) was easily converted into different MnO_x crystalline structures ($\text{MnO}_x@\text{CNF}$) by mild thermal treatment. This strategy has the merit to keep the amount of conformal deposit on CNFs the same (and so with a same amount of Mn element whatever the thermal treatment) while controlling the average oxidation state of Mn through temperature.⁴¹ Additionally, the electrode architecture remains unchanged thanks to the conductive and mechanically robust skeleton of the 3D CNFs, thus guaranteeing identical access to the electrolyte components whatever the nature and structure of the deposit. With this approach, we were able to perform a quantitative study of each of the MnO_x crystalline structures, including the spinel Mn_3O_4 structure ($\text{Mn}_3\text{O}_4@\text{CNF}$) as well as the pristine deposit of amorphous MnO_2 . The MnO_x structures on CNFs were investigated in various mild buffered and unbuffered aqueous electrolytes, by focusing on the first galvanostatic discharge or the first galvanostatic charge-discharge cycle, complemented by *ex-situ* characterization by X-ray diffraction (XRD), scanning electron microscopy (SEM), high-resolution transmission electron microscopy (HRTEM), and X-ray photoelectron spectroscopy (XPS). As will be discussed below, our results demonstrate that a universal charge storage mechanism is at work, relying on a full proton-coupled electrodisolution of the solid MnO_x material into soluble Mn^{2+} , regardless of the crystallinity and valence state of the MnO_x structures as well as nature of the aqueous electrolyte (*i.e.*, either it is buffered or unbuffered).

2. Results and discussions

2.1. Preparation of amorphous $\text{MnO}_2\text{@CNF}$ and crystalline $\text{MnO}_x\text{@CNF}$ electrodes

2.1.1. Amorphous $\text{MnO}_2\text{@CNF}$

Polyacrylonitrile (PAN) derived free-standing 3D CNF substrates were prepared by electrospinning technique and subsequent carbonization at 1200°C under steady-state Ar flow, as reported earlier.^{44,45} The field emission gun SEM (FEG–SEM) and HRTEM images of CNF show that nanofibers possess a smooth non-porous surface with an average diameter of 127 ± 47 nm (see Fig. S1 in Electronic Supplementary Information (ESI)). The MnO_2 coatings on the disk-shaped CNF electrodes were prepared by galvanostatic electrodeposition from an aqueous buffered solution containing Mn^{2+} and the application of a total load (Q_T) of 1 C/cm^2 (graph C in Fig. S1). This loading value was selected on the basis of our previous work, showing that the CE remains quite good (97%) when the load is lower than 3 C/cm^2 .⁴⁵ Fig. 1A shows the XRD pattern of the amorphous $\text{MnO}_2\text{@CNF}$ electrode, presenting two broad peaks at $2\theta = 24.8^\circ$ and 37° . The former is the characteristic (002) plane of the amorphous CNFs, exhibiting short-range ordered (graphitic) domains,⁴⁶ while the latter represents the poorly crystalline structure of the electrodeposited MnO_2 film.⁴⁷ The FEG-SEM image (Fig. 1B) shows a conformal, uniform, and highly porous MnO_2 film, made of sheet-like nanostructures arranged perpendicular to the CNF surface. The HRTEM imaging with its elemental (Mn, O) maps in Fig. 1C and the dark-field scanning transmission electron microscopy (STEM) image with a selected area electron diffraction (SAED) pattern in Fig. S2, further confirm the sheet-like amorphous MnO_2 structures on CNF. The thickness of the MnO_2 coating is between 40–50 nm, as inferred from the line-scanning elemental mapping (C, Mn, O) in Fig. S3. The average oxidation state (AOS) of Mn was estimated from the core-level Mn 3s XPS spectra as shown in Fig 1G. It is found to be 3.68, based on the energy separation peaks ΔE of 4.66 eV, which translates into a load of $\sim 0.54 \text{ mg}_{\text{MnO}_2}/\text{cm}^2$ if we assume an average transfer of $n = 1.68$ e^- per Mn element during the electrodeposition process. The AOS of Mn agrees with the values previously reported for either galvanostatic or potentiostatic deposition of MnO_2 (or more rigorously of $\text{Mn}^{\text{IV}}_{1-x-y}\text{Mn}^{\text{III}}_y\text{O}_2\text{K}_z\text{H}_{4x+y-z}$ if we consider that the electrodeposited MnO_2 contains a few Mn^{III} as well as Mn^{IV} vacancies \square) under comparable^{11,45,48} or somewhat different experimental conditions.^{14,49,50}

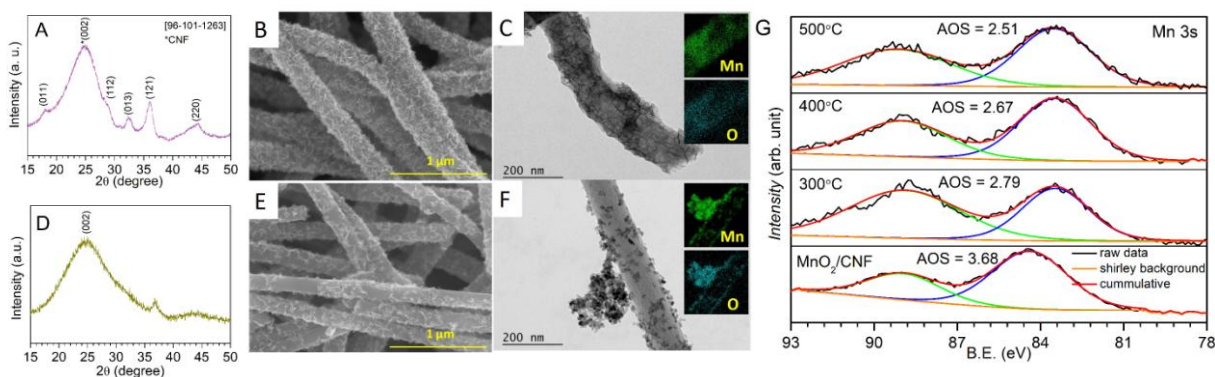


Fig. 1. XRD patterns, FEG-SEM image, and HRTEM images (including the elemental (Mn, O) maps in the inset) obtained for (A-C) the as-deposited MnO₂@CNF sample and (D-F) spinel Mn₃O₄@CNF sample heated at 400°C. (G) Core-level Mn 3s spectra of MnO_x@CNF samples for the pristine MnO₂ material and the MnO_x phases obtained at different thermal annealing temperatures.

2.1.2. Crystalline MnO_x@CNF

For the preparation of the crystalline MnO_x structures (including thus the spinel Mn₃O₄ structure) on CNFs (also referred as MnO_x@CNF), the as-deposited amorphous MnO₂@CNF samples were washed thoroughly in deionized water and subsequently heated at various temperatures (ranging from 300 to 500°C) for 1 h under a steady-state flow of argon. Upon heating at 400°C, the amorphous MnO₂ transforms into a crystalline structure in which the initial high mixed-valence oxidation state of Mn (AOS of 3.68) reduces to a lower mixed-valence tetragonal spinel Mn₃O₄ structure, as evidenced by the diffraction peaks in Fig. 1D which index well to this structure (see JCPDS file no 96-101-1263). While no other crystalline phases are observed in the Mn₃O₄@CNF XRD pattern, the retention of some minor fraction of amorphous MnO₂ and/or MnO_x cannot be excluded. The broadening of the diffraction peaks is due to the typically inherent nanosized polycrystalline structures.⁵¹ The mean size of the ordered (crystalline) domain (τ) calculated from the Scherrer formula for the most intense (121) peak is found to be ~13 nm. The HRTEM imaging with elemental (Mn, O) maps shows that upon heating, sheet-like MnO₂ nanostructures are mostly converted into Mn₃O₄ nanoparticles and/or larger structures made of interconnected Mn₃O₄ nanoparticles (Fig. 1F). The average size of Mn₃O₄ nanoparticles estimated from the HRTEM image is 10.6 ± 2.1 nm, close to the crystallite size calculated from the XRD spectra. Furthermore, the interplanar spacing of Mn₃O₄ nanoparticles estimated from the dark-field STEM image is 2.7618 Å (Fig. S4), which is in agreement with the typical d -spacing of the (013) plane of a tetragonal Mn₃O₄ spinel structure. The SAED pattern shows Bragg-reflection spots making a

pattern of rings (Fig. S4), further confirming the polycrystalline nature of randomly oriented nanosized Mn_3O_4 particles and corroborating the XRD results.

Tracking by *ex-situ* XRD the progress of phase conversion from amorphous MnO_2 to spinel Mn_3O_4 reveals that the poorly ordered pristine MnO_2 phase progressively transforms to a crystalline spinel Mn_3O_4 phase when heated $\geq 400^\circ\text{C}$ (Fig. S5), while heating at a higher temperature of 500°C leads to the further appearance of a minor MnO phase (JCPDS file no 96-101-0394). FEG-SEM images of all samples also indicate that, within the resolution of this technique, there are no/little changes in the morphology of MnO_x structures upon heating (Fig. S6). The AOS of Mn deduced from XPS for each $\text{MnO}_x@\text{CNF}$ electrode (Fig. 1G) reveals that the initial AOS value of 3.68 is reduced to 2.79, 2.67, and 2.51 after thermal treatment at 300°C , 400°C , and 500°C , respectively. This is due to the loss of oxygen from the crystal structure and concomitant reduction of Mn^{IV} centers into a mix of Mn^{III} and Mn^{II} ($3 \text{ MnO}_2 \rightarrow \text{Mn}_3\text{O}_4 + \text{O}_2$).^{52,53} The sample prepared at 400°C thus appears as the one with the closest AOS value to that expected for a pure Mn_3O_4 phase ($\text{Mn}^{\text{II}}\text{Mn}^{\text{III}}_2\text{O}_4$ with theoretical AOS = 2.67).

2.2. Galvanostatic discharge of crystalline $\text{MnO}_x@\text{CNF}$ electrodes

2.2.1. First discharge in an acidic aqueous electrolyte

Amorphous $\text{MnO}_2@\text{CNF}$ and crystalline low-valence $\text{MnO}_x@\text{CNF}$ electrodes (notably $\text{Mn}_3\text{O}_4@\text{CNF}$) were characterized electrochemically by galvanostatic cycling in a two-electrode Swagelok cell against a Zn foil anode. The $\text{MnO}_x@\text{CNF}$ electrodes were first discharged in an aqueous electrolyte of pH 1.7, containing 1.3 m $\text{Al}(\text{OTf})_3$ along with 0.3 M MnCl_2 . This electrolyte was selected because it was previously shown by us to be an efficient media for the proton-coupled reductive electrodisolution of amorphous MnO_2 to soluble Mn^{2+} .¹⁶ We confirm here this good efficiency with the as-prepared $\text{MnO}_2@\text{CNF}$ electrode (Fig. 2A), showing from the first galvanostatic discharge a well-defined single plateau at ~ 1.5 V, characteristic of a full two-electron faradaic electrodisolution of the amorphous MnO_2 into soluble Mn^{2+} . This full electrodisolution of the active material is corroborated by the total discharge capacity (Q_d) of 992 mC/cm^2 , which is close to the Q_T load of 1 C/cm^2 used for the preparation of $\text{MnO}_2@\text{CNF}$ electrodes (leading thus to a *CE* of 99.2%). Additionally, the *ex-situ* XRD and FEG-SEM analyses of the discharged electrode (Fig. S5 and S6) indicate a complete loss of the active material. In comparison, the first galvanostatic discharges recorded for the $\text{MnO}_x@\text{CNF}$ electrodes in the same electrolyte present a much shorter plateau localized at a slightly higher potential ($E_d \sim 1.7$ V) (Fig. 2A). These shorter plateaus demonstrate an intrinsic lower capacity of the low-valence MnO_x structures

compared to the pristine MnO_2 . Furthermore, the discharge capacity decreases from 475 to 283 mC/cm^2 as the thermal heating temperature used to convert the as-electrodeposited amorphous MnO_2 to a crystalline MnO_x structure increases from 300 to 500°C. Plotting the experimental Q_d value obtained for each $\text{MnO}_x\text{@CNF}$ electrode as a function of the AOS of Mn (Fig. 2B) reveals that it scales linearly with the valence of Mn in the MnO_x material. On the same graph is also reported, for each electrode, the CE obtained from the ratio between the experimental capacity, Q_d , and the maximal theoretical discharge capacity, $Q_{d,\text{th}}$, the latter being calculated using eq. 1 (assuming the complete reduction of MnO_x into a Mn^{II} -based compound).

$$Q_{d,\text{th}} \left(\text{C/cm}^2 \right) = Q_T \times \left(\text{AOS}_{\text{MnO}_x} - 2 \right) / \left(\text{AOS}_{\text{MnO}_2} - 2 \right) \quad (1)$$

(where $Q_T = 1 \text{ C/cm}^2$, $\text{AOS}_{\text{MnO}_2} = 3.68$, and $\text{MnO}_x = 2.79, 2.67$, or 2.51). The resulting CE s are all above 90%, demonstrating that for all $\text{MnO}_x\text{@CNF}$ electrodes the Mn element is almost completely reduced to the Mn^{II} state after the first discharge.

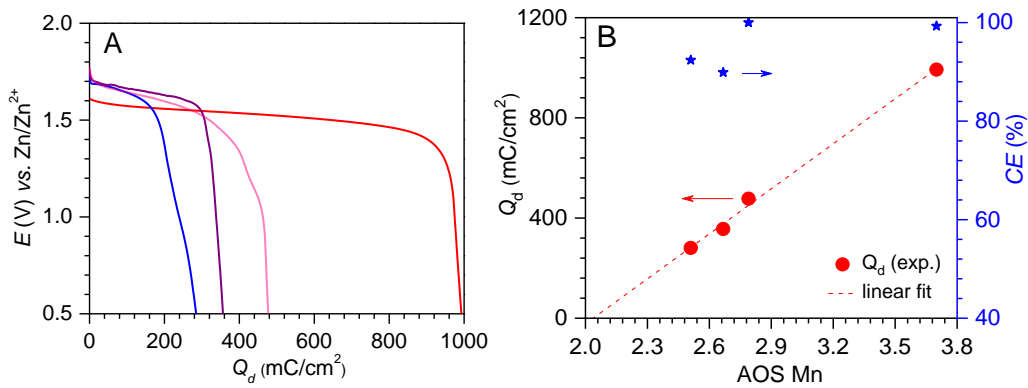


Fig. 2. (A) First galvanostatic discharges (-0.6 mA/cm^2) recorded at different $\text{MnO}_x\text{@CNF}$ electrodes in a 1.3 m $\text{Al}(\text{OTf})_3$ aqueous electrolyte containing 0.3 M Mn^{2+} (pH 1.7). The first discharges of different $\text{MnO}_x\text{@CNF}$ electrodes were obtained as follows: (red) as-deposited without thermal treatment, and after heating at (pink) 300°C, (purple) 400°C, and (blue) 500°C for 1 h under a steady-state flow of argon. (B) a plot of the experimental Q_d recovered from the first discharges in A. The dotted lines represent the linear regression to the experimental data ($r^2 \geq 0.99443$). The CE in blue represents the ratio between the experimental capacity, Q_d (recovered from graph A) and the maximal theoretical discharge capacity, $Q_{d,\text{th}}$ (calculated from the AOS of Mn according to eq. 1).

Ex-situ XRD analyses of the discharged electrodes confirm the loss of all MnO_x structures (see Fig S5), while the complete reduction of MnO_x into Mn^{II} (and more specifically into soluble Mn^{2+}) is confirmed by the FEG-SEM images of the discharged electrodes (almost all of the MnO_x coatings have disappeared from the surface of CNFs – see Fig. S6). These observations finally demonstrate that the electrochemical discharge mechanism of MnO_x @CNF electrodes in the acidic Al^{3+} -based electrolyte relies on a proton-coupled electrodisolution process, analogous to that we had previously established for amorphous MnO_2 .¹⁶ This result goes against publications claiming that the discharge mechanism of MnO_x structures in Al^{3+} -based electrolytes involves the reversible insertion of Al^{3+} cations in the metal oxide⁵⁴⁻⁵⁷ The electrodisolution of MnO_x compounds in a slightly acidic electrolyte is not a surprise since, according to the Mn Pourbaix diagram, Mn^{2+} is thermodynamically the stable reduction state at $\text{pH} < 7$.⁵⁸ Previously, we established the key role of proton donor played by the weak acid hexaaquo Al^{3+} complex ions (*i.e.*, $[\text{Al}(\text{H}_2\text{O})_6]^{3+}$, $\text{pK}_a = 4.95$) in the proton-coupled electrochemical reduction of metal oxides (*i.e.*, either TiO_2 or MnO_2).^{16,59} By extension, we can argue here that the same $[\text{Al}(\text{H}_2\text{O})_6]^{3+}$ ions are involved as proton donors to trigger the electrochemical dissolution of the different MnO_x active materials.

2.2.2. First discharge of Mn_3O_4 @CNF in mild aqueous electrolytes

We next focused our attention on the electrochemical behavior of the spinel Mn_3O_4 @CNF electrode (prepared at 400°C , and referred as Mn_3O_4) under mild pH conditions. We first investigated the discharge in an acetate buffered electrolyte (2 M, pH 4.7) which allows to keep the pH approximately constant at the electrode/electrolyte interface during the whole discharge. An interest of the acetate buffer is that the acetic acid has a comparable weak Brønsted acidity ($\text{pK}_a = 4.76$) than $[\text{Al}(\text{H}_2\text{O})_6]^{3+}$ ($\text{pK}_a = 4.97$ ⁶⁰). Moreover, at pH 4.7, the hydronium ions concentration remains negligible ($[\text{H}_3\text{O}^+] \approx 10^{-5}$ M), which means that free protons cannot contribute significantly to the electrochemical process. To this buffer, 0.3 M of Mn^{2+} (MnCl_2) was also added as an additive (*vide infra*). As shown in Fig. 3A (olive curve), the first galvanostatic discharge of the Mn_3O_4 @CNF electrode leads to a well-defined single plateau with a discharge capacity of $Q_d = 393 \text{ mC/cm}^2$, a value that is very close to the theoretical one (*i.e.*, $Q_{d,\text{th}} = 402 \text{ mC/cm}^2$, estimated from the Mn AOS of Mn_3O_4 , *i.e.* 2.67). This suggests that Mn_3O_4 is completely electrochemically reduced up to the Mn^{II} oxidation state. Compared to the more acidic Al^{3+} -based electrolyte, the discharge potential is here slightly shifted to a lower value, with a tendency to decrease more steeply during the course of the discharge (*i.e.*, the discharge is less flat). Reproducing the experiment in the same

buffered electrolyte but free of Mn^{2+} leads to an almost identical discharge curve (dark yellow plot in Fig. 3A), demonstrating that the presence of Mn^{2+} in the electrolyte does not significantly disturb/influence the discharge process. FEG-SEM imaging of the discharged electrode confirms a full electrodisolution of the spinel Mn_3O_4 compound (Fig. 3C), which again allows to conclude to a proton-coupled electrodisolution of the Mn_3O_4 crystalline phase (identical thus to the above results obtained in the more acidic Al^{3+} -based electrolyte).

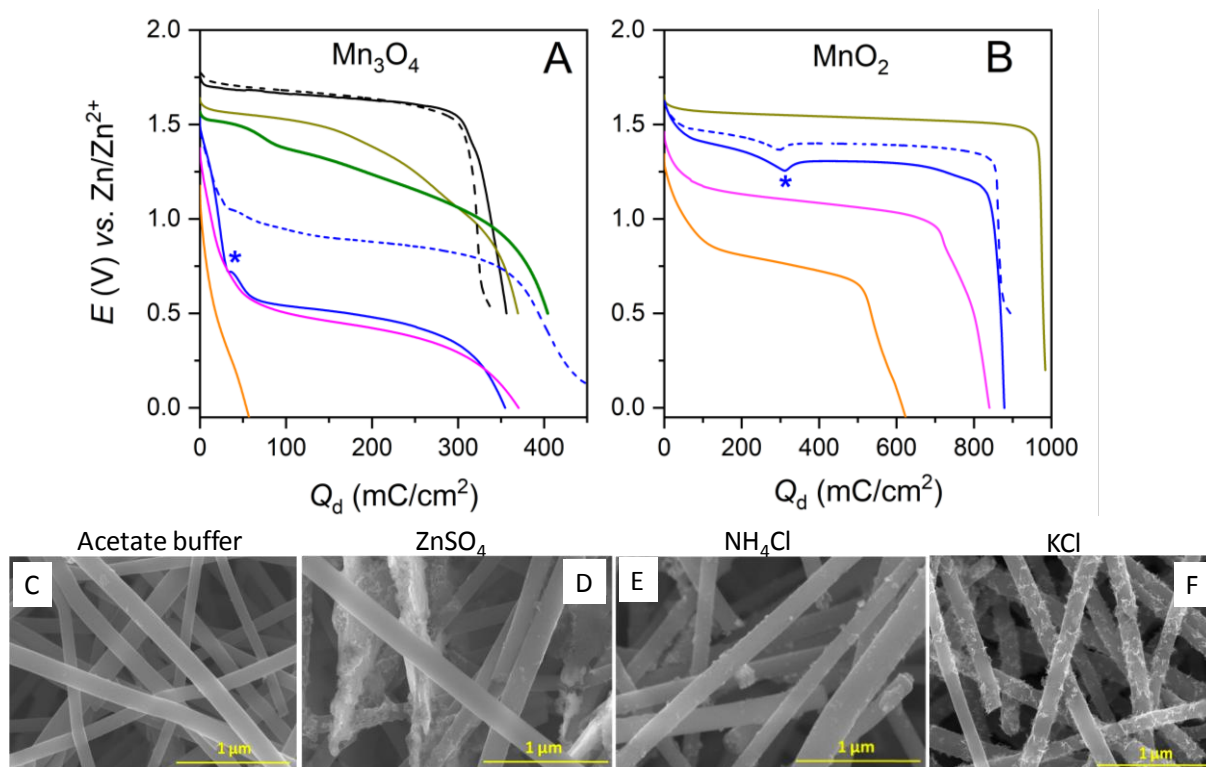


Fig. 3. (Top) First galvanostatic discharge of (A) Mn_3O_4 @CNF and (B) amorphous MnO_2 @CNF electrodes in aqueous electrolytes containing: (black) 1.3 m $\text{Al}(\text{OTf})_3$ (pH 1.7), (olive) 2 M acetate buffer + 0.3 M Mn^{2+} (pH 4.7), (dark yellow) 2 M acetate buffer (pH 4.7), (blue) 1 M ZnSO_4 (pH 4.2), (magenta) 1 M NH_4Cl (pH 5.1), and (orange) 1 M KCl (pH 6.08). The discharge rates were (plain lines) -0.6 and (dashed lines) $-0.012 \text{ mA}/\text{cm}^2$. (Bottom) FEG-SEM images of the Mn_3O_4 @CNF after completion of the first discharge in a: (C) 2 M acetate buffer, (D) 1 M ZnSO_4 , (E) 1 M NH_4Cl , and (F) 1 M KCl electrolyte.

To better highlight the crucial role played by the acetate buffer in the faradaic discharge process, we have repeated the experiment in an unbuffered 1 M KCl electrolyte (pH ~ 6.0). Under these conditions, the discharge of the Mn_3O_4 @CNF electrode presents a rapid steady decrease of the potential, with no discernable plateau within the potential window explored (orange plot in Fig. 3A). This finally leads to a very low total discharge capacity ($\sim 55 \text{ mC}/\text{cm}^2$). This behavior is characteristic of an almost exclusive double-layer capacitive

discharge,¹¹ which demonstrates that in the absence of buffer (or more rigorously in the absence of a sufficiently acidic proton donor), the faradaic proton-coupled electrodisolution of Mn_3O_4 cannot take place (this is confirmed by the FEG-SEM image of the discharged electrode in Fig. 3F, which shows that the CNFs remain coated by the Mn_3O_4 material). Nevertheless, this behavior is specific to Mn_3O_4 since amorphous MnO_2 under same conditions leads to a significant discharge plateau at *ca.* 0.8 V (Fig. 3B), we can attribute to the electrodisolution of MnO_2 to Mn^{2+} , assisted this time by the protons supplied by water (*i.e.*, $\text{MnO}_2 + 2 \text{H}_2\text{O} + 2 \text{e}^- \rightleftharpoons \text{Mn}^{2+} + 4 \text{OH}^-$).

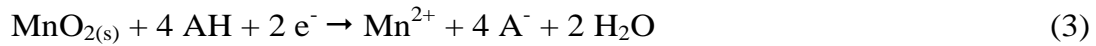
Having established that in a mild-aqueous acetate buffer, the first discharge leads to the complete removal of the active material from CNFs by electrodisolution, the next question that was interesting to address is what is the discharge mechanism when working now in an unbuffered Zn^{2+} -based mild aqueous electrolyte (*i.e.*, conditions generally met in aqueous Zn/MnO_x batteries). Fig. 3A (plain blue plot) shows the galvanostatic discharge of a $\text{Mn}_3\text{O}_4@\text{CNF}$ electrode in a 1 M aqueous ZnSO_4 (pH \sim 4.2). In contrast to the discharge curves performed in the acetate buffer at the same rate (*i.e.*, -0.6 mA/cm^2), a large voltage drop is here observed at the beginning, until it stabilizes and leads to a well-defined discharge plateau at \sim 0.50 V (the latter accounting for *ca.* 80% of the total discharge). FEG-SEM analysis of the discharged electrode (Fig. 3D) shows that almost all of the Mn_3O_4 has disappeared from the CNF surface (the image shows clean CNF with the presence of a precipitate in between the fibers, which corresponds to a zinc double hydroxide precipitate – *vide infra*). This latter indicates that the active material has almost fully electrodisolved during the discharge. This is corroborated by the EDS analysis showing a very low atomic % of Mn on the discharge electrode (Fig. S7). Further, the total discharge capacity (355 mC/cm^2) is close to the theoretical one ($CE = 89\%$). The same experiment reproduced at a lower rate (*i.e.*, -0.012 mA/cm^2) leads to an up-shift of the discharge curve to more positive voltages (blue dashed plot in Fig. 3A). Still, full electrodisolution of Mn_3O_4 is confirmed from the FEG-SEM images and EDS mapping (Fig. S8). Additionally, the XRD pattern (Fig. S9) of the slowly discharged electrode is characterized by a very weak Mn_3O_4 signal as well as the appearance of new peaks at $2\theta = 16.8^\circ$ and 33.2° (intense peak). These peaks are indexed to a Zn^{II} layered double hydroxide phase,²² and, probably, to a $\text{Zn}_4(\text{OH})_6\text{SO}_4 \cdot 4\text{H}_2\text{O}$ (ZHS) phase according to the JCPDS PDF no 44-0673⁶¹ and elemental mapping (Fig S8). The presence of this precipitate suggests the rise of pH close to the electrode, a behavior that is corroborated by the large voltage drop observed at the beginning of the discharge curve, thereby signing the pH dependence of the discharge potential (E_d). This pH increase can be easily understood

if we consider that the discharge mechanism is a proton-coupled electrodisolution process, thus requiring several equivalents of protons (or proton donors) for taking place.¹¹ As a result, under the unbuffered conditions of the ZnSO₄ electrolyte, the local consumption of protons by the electrochemical reaction leads to a local rise in pH and then, at some point, to the precipitation of the zinc double hydroxide at the electrode/electrolyte interface. The formation of a zinc hydroxide precipitate upon cycling a MnO_x cathode in a ZnSO₄ electrolyte is a phenomenon that has been reported in a large number of works.^{17,22,24,41,58,62-66} However, this process is often assumed to be linked to the insertion/intercalation of protons within the reduced active material,^{4,17,41,61,67,68} which is different from the proton-coupled electrodisolution mechanism proposed here. Many studies also report that regardless of the mechanism (*i.e.*, whether it is based on a proton insertion into MnO_x or a proton-coupled electrodisolution of MnO_x), the protons arise from water.^{4,13,14,17,18,64,69} However, this cannot explain the absence of a proton-coupled faradaic process when the Mn₃O₄ electrode is discharged in 1 M KCl aqueous electrolyte (see above and also ref. 11). As we have previously shown, the reason for the existence of a proton-coupled faradaic process (and so of a plateau) in a ZnSO₄ electrolyte is due to the presence of the hexaaquo complex of Zn²⁺ (*i.e.*, [Zn(H₂O)₆]²⁺).¹¹ This aquo metal ion is characterized by a well-known weak Brønsted acidity (related to two p*K_a*s close to 9.0),⁷⁰ which is lower than for [Al(H₂O)₆]³⁺ (see above) but sufficient to trigger the proton-coupled electrodisolution of MnO_x. Once two protons are removed from [Zn(H₂O)₆]²⁺, the resulting neutral Zn^{II} double hydroxide precipitates (also probably accompanied by the co-precipitation of a Mn^{II} double hydroxide as it was demonstrated in ref. 22). The precipitation can be visualized on the discharge curves by a voltage dip (marked by a blue asterisk on the blue discharge plots of Fig. 3A and 3B), coinciding to the beginning of the nucleation and growth of the precipitate.⁶⁶ This voltage dip is immediately followed by a rather stable discharge plateau, which is characteristic of the steady precipitation of the zinc hydroxide with concomitant stabilization of the local pH.⁶⁶ It is interesting to note that the voltage dip on the discharge curve of the Mn₃O₄@CNF electrode is not localized at the same voltage/time position as the pristine MnO₂@CNF electrode, indicating that the beginning of the precipitation differs for each material.

To further confirm the key role of [Zn(H₂O)₆]²⁺ in the proton-coupled electrodisolution mechanism of Mn₃O₄, we next monitored the first discharge in a 1 M NH₄Cl aqueous electrolyte (pH 5.1). This unbuffered electrolyte was selected because NH₄⁺ exhibits a similar weak Brønsted acidity (p*K_a* = 9.2) than [Zn(H₂O)₆]²⁺, having thus an equivalent acidity strength. As shown in Fig. 3A, apart from the absence of a voltage dip in the curve (which *a*

priori indicates the absence of precipitate formation), the discharge curve in NH_4Cl (magenta plot) is almost overlapping with the one previously recorded in ZnSO_4 (blue plot). FEG-SEM analysis of the fully discharged electrode indicates only residual Mn_3O_4 on the CNFs with no evidence of a precipitate (see Fig. 3E), which thus agrees with a full proton-coupled electrodisolution of Mn_3O_4 in the presence of NH_4^+ , occurring without precipitation in spite of a rise in the local pH. This result finally confirms that with a $\text{p}K_a$ of ~ 9 , a weak Brønsted acid such as NH_4^+ or $[\text{Zn}(\text{H}_2\text{O})_6]^{2+}$ is acidic enough to trigger the complete reductive electrodisolution of Mn_3O_4 .

By comparing the discharge curves recorded in the acetate buffer (dark yellow plot in Fig. 3A) with those recorded in the unbuffered aqueous ZnSO_4 (blue plot in Fig. 3A), one can notice a very significant difference in the discharge potential (around 1 V difference) despite an identical bulk pH for both electrolytes. Moreover, this difference in E_d is much larger with the crystalline spinel Mn_3O_4 phase than with the amorphous MnO_2 (compare the dark yellow and blue plots in Fig. 3B). At first sight, we can assume that these distinct electrochemical behaviors are the consequence of the different stoichiometries (notably the proton/electron ratio) of the two electrodisolution reactions, *i.e.*:



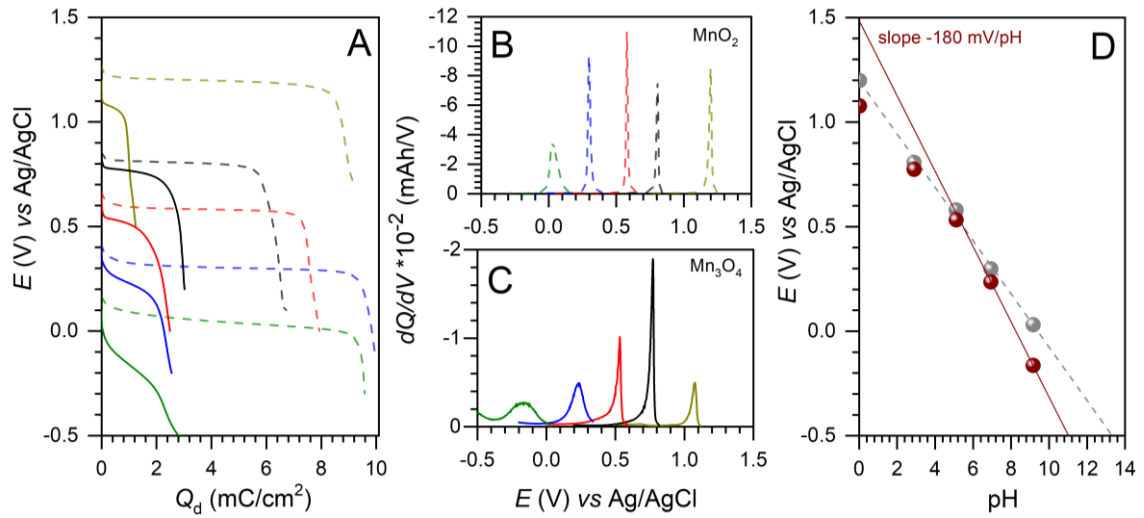
where AH and A^- are, respectively, the weak acid and weak conjugate base present (and/or electrogenerated) in the electrolyte.

Given the different stoichiometry of these two reactions, it was interesting to investigate the pH dependence of the discharge potential. To do so, we conducted a series of experiments on 2D transparent FTO electrodes coated with thin films of MnO_2 or Mn_3O_4 (see SI for details). These model electrodes were prepared following identical protocols to those used for $\text{MnO}_2@\text{CNF}$ and $\text{Mn}_3\text{O}_4@\text{CNF}$ electrodes. After heating at 400°C , an AOS of Mn of 2.65 was determined by XPS (Fig. S10), attesting to the formation of Mn_3O_4 on the FTO substrate. The first galvanostatic discharges of these model electrodes were recorded (in a 3-electrode setup¹¹) in aqueous buffers of different pHs, ranging from 2.9 to 9.2, and also in an acidic 1.5 M HCl solution (Fig. 4). The galvanostatic discharge experiments were also performed at a slow rate in order to be as close as possible to the thermodynamic equilibrium. By this way,

the experimental E_d of either Mn_3O_4 or MnO_2 is assumed to follow the pH-dependent Nernst eq. 4 or 5 associated with reaction 2 or 3, respectively:

$$E_{eq} = E_{\text{Mn}_3\text{O}_4/\text{Mn}^{2+}}^0 - 0.24 \text{ pH} - 0.09 \log(a_{\text{Mn}^{2+}}) \quad (4)$$

$$E_{eq} = E_{\text{MnO}_2/\text{Mn}^{2+}}^0 - 0.12 \text{ pH} - 0.03 \log(a_{\text{Mn}^{2+}}) \quad (5)$$



where E_{eq} is the equilibrium potential, $E_{\text{Mn}_3\text{O}_4/\text{Mn}^{2+}}^0$ the standard potential of the $\text{Mn}_3\text{O}_4/\text{Mn}^{2+}$ redox couple (1.824 vs. NHE⁷¹), $E_{\text{MnO}_2/\text{Mn}^{2+}}^0$ the standard potential of the $\text{MnO}_2/\text{Mn}^{2+}$ redox couple (*i.e.*, 1.315 V vs. NHE for γ - MnO_2 ⁷²), and $a_{\text{Mn}^{2+}}$ the activity of Mn^{2+} at the electrode vicinity.

Fig. 4. (A) First galvanostatic discharges recorded at $-50 \mu\text{A}/\text{cm}^2$ for MnO_2 @FTO (dashed lines) and Mn_3O_4 @FTO (plain lines) electrodes in aqueous 1.5 M HCl (pH 0.0; dark yellow), 0.9 M chloroacetate buffer (pH 2.9; black), 1.0 M acetate buffer (pH 5.1; red), 0.45 M HEPES buffer (pH 6.9; blue), and 0.66 M ammonium buffer (pH 9.2; olive). (B-C) dQ/dV (differential capacity) of amorphous MnO_2 /FTO and crystalline Mn_3O_4 /FTO electrodes as a function of their discharge potential. (D) Average discharge potentials (*i.e.*, peak potentials in dQ/dV analysis) plotted as a function of bulk pH of the solution for (grey) MnO_2 and (red) Mn_3O_4 .

The E_d values recovered from the galvanostatic discharges of pristine MnO_2 @FTO electrodes (or also derived more accurately from the plots of the differential capacity shown in Fig. 4B

and 4C^\ddagger) show, as expected, a linear dependence on pH, with a slope of -127 mV/pH unit and an intercept of 1.20 V (vs. Ag/AgCl, or 1.39 V vs. NHE) (Fig. 4). These values perfectly agree with eq. 5 and thus indicate that whatever the pH, the electrodisolution of MnO_2 is primarily governed by thermodynamics under the selected experimental conditions.⁴⁴

In the case of the Mn_3O_4 @FTO electrodes, E_d values are also pH dependent, attesting to the role of protons in the electrochemical discharge reaction of Mn_3O_4 . However, while nearly stable plateaus and sharp dQ/dV peaks were acquired at pHs < 6.0 (reminiscent of those recorded at MnO_2 over the entire pH range), sloppy discharges and broad dQ/dV peaks were obtained at pHs > 6.0. Furthermore, the plot of E_d as a function of pH deviates from linearity (Fig. 4D). This suggests that the mechanism of Mn_3O_4 electrodisolution varies with the pH. We emitted the hypothesis that it could be the consequence of the lack of chemical stability of Mn_3O_4 in acidic media. We have thus analyzed the chemical stability of the Mn_3O_4 @FTO electrodes by simply soaking them for 15 minutes in a range of electrolytes of different pH, and then determined by *ex-situ* XPS the AOS of Mn, and by XRF analysis the remaining amount of Mn on FTO (see SI for details). The results manifest that the Mn_3O_4 coating spontaneously evolves in the most acidic electrolytes (*i.e.*, in the 1.5 M HCl of pH 0 and 1.3 M $\text{Al}^{3+} + 0.3 \text{ M Mn}^{2+}$ of pH 2.0), leading to a significant decrease of Mn on the electrode surface (~50% loss) as well as a concomitant increase of the AOS of the remaining Mn up to 3.3 (see Fig S11). These results are in agreement with the increasingly favorable dismutation of the Mn^{III} ions in the Mn_3O_4 lattice as the pH is lowered, a dismutation reaction that can be described by the following chemical equilibrium:⁷³



The consequence of such *in-situ* dismutation of Mn_3O_4 to MnO_2 is that the discharge curves in the most acidic electrolytes behave closely or equivalently to those recorded at MnO_2 electrodes, thus leading to a same E_d and pH dependency (*i.e.*, -120 mV/pH unit, as indicated by the parallel plots of Mn_3O_4 and MnO_2 at pHs < 4) (Fig. 4D).[§] *On contrario*, Mn_3O_4 is much more stable in mild to neutral aqueous electrolytes. Indeed, Mn_3O_4 @FTO electrodes soaked under open circuit for 15 min in a 1 M acetate buffer showed only minor changes in the AOS of Mn as well as in the amount of Mn on the FTO substrate. This is even better with the electrodes soaked in a 1 M ZnSO_4 electrolyte, for which almost no change is observed (Fig. S11). From the linear regression fit of the two less acidic pHs in Fig. 5, a slope of -180 mV/pH unit and an intercept of 1.49 V (vs. Ag/AgCl or 1.68 V vs. NHE) are extracted. These

values are finally close to those predicted for the proton-coupled electrodisolution of Mn_3O_4 (see eq. 4). In conclusion, the nonlinear pH dependence of E_d reported for Mn_3O_4 in Fig. 4D reflects a change in the electrodisolution mechanism, which can be rationalized by the increased dismutation of Mn_3O_4 to MnO_2 when switching from neutral to acidic pH. If we consider now that the discharges curves recorded at $\text{pH} > 6.0$ pertain to the electrochemical reduction of Mn_3O_4 , it is interesting to notice that they display a more sluggish behavior than MnO_2 (which is also revealed from the broader dQ/dV peaks in Fig. 4C). This likely indicates an inherently slower reactivity of the Mn_3O_4 crystal structure, an observation that is consistent with the low electrochemical reactivity of Mn_3O_4 under neutral or basic conditions (we recall here that the short cycle life of Zn- MnO_2 alkaline batteries is thought to stem from the low electroactivity of Mn_3O_4 that accumulates during cycling).^{74,75}

The conclusions drawn here from the analysis of the model electrodes are transposable to the $\text{Mn}_3\text{O}_4@\text{CNF}$ electrodes and fully consistent with the shape and potential position of the $\text{Mn}_3\text{O}_4@\text{CNF}$ discharge curves. In the acidic Al^{3+} -based electrolyte ($\text{pH} 1.7$), they are close to those obtained for the pristine $\text{MnO}_2@\text{CNF}$ in the same electrolyte, which is fully consistent with the assumption of *in-situ* dismutation of Mn_3O_4 to MnO_2 (Fig. 2). It is also corroborated by the rather small influence of the rate on the discharge curve of $\text{Mn}_3\text{O}_4@\text{CNF}$ (Fig. 3A) in the acidic Al^{3+} -based electrolyte ($\text{pH} 1.7$), which does not correlate with the slow electrochemical reactivity expected for Mn_3O_4 . *On contrario*, in the less acidic ZnSO_4 electrolyte ($\text{pH} 4.2$), the shape and the potential position of the $\text{Mn}_3\text{O}_4@\text{CNF}$ discharge curves are clearly different from those of the pristine $\text{MnO}_2@\text{CNF}$ electrode, which thus supports that we are now predominantly dealing with a mechanism characteristic of the Mn_3O_4 discharge. Such conditions thereby allow to unambiguously access to the true thermodynamics and kinetics of Mn_3O_4 electrodisolution. We can infer that its E_d value is definitely localized at a much lower value than that of MnO_2 under mild to neutral pH conditions (compare the blue plots of graphs A and B in Fig. 3), which is consistent with what is predicted by eqs. 4 and 5 (giving identical E_{eq} values for $\text{pH} 4.2$). Furthermore, the stronger influence of the rate on the discharge curve of Mn_3O_4 (Fig. 3) reflects slower kinetics of the proton-coupled electrodisolution of crystalline Mn_3O_4 compared to amorphous MnO_2 .

In conclusion, all these observations indicate that in a mild aqueous ZnSO_4 electrolyte, the relatively stable spinel Mn_3O_4 material discharges through a universal proton-coupled electrodisolution mechanism, wherein the protons are brought by the solvated Zn^{2+} ions in the electrolyte. This mechanism is only accessible during the first discharge because once the solid Mn_3O_4 is totally converted into soluble Mn^{2+} , it is obviously not possible to come back

by electrodeposition to the original Mn_3O_4 crystalline structure (see in SI the note on the cyclability of $\text{Mn}_3\text{O}_4@\text{CNF}$ in a mild buffered electrolyte).

2.3. Electrochemical oxidative activation of $\text{Mn}_3\text{O}_4@\text{CNF}$ electrode in mild-aqueous electrolytes

We next turned our attention to the intriguing and poorly understood slow electrochemical oxidative activation of Mn_3O_4 (leading to a gradual capacity increase upon cycling) that was previously reported in several works when working in mild aqueous electrolytes.^{30,31,36,37,40,42,43} This electrochemical activation also echoes a similar behavior observed with the low valence spinel structure of ZnMn_2O_4 .⁴¹ In their paper of 2018, Hao *et al.* concluded that, during its charge, Mn_3O_4 slowly electrochemically oxidizes to an intermediate Mn_5O_8 phase which further transforms to birnessite MnO_2 after several activation cycles in a ZnSO_4 electrolyte.³⁰ This conversion of Mn_3O_4 into Mn_5O_8 was however not observed by Wilkinson's group in the same electrolyte,³⁶ which instead concluded that complete transformation of Mn_3O_4 to MnO_2 upon continuous cycling requires the presence of both Zn^{2+} and protons, both being associated to the formation of Zn-species at the electrode. In an attempt to clarify this point, we examined the electrochemical activation of the $\text{Mn}_3\text{O}_4@\text{CNF}$ electrodes in both a 1 M ZnSO_4 electrolyte (pH \sim 4.2) and 2 M acetate buffer (pH 4.7) without pre-added Mn^{2+} . For this purpose, freshly prepared $\text{Mn}_3\text{O}_4@\text{CNF}$ electrodes were galvanostatically cycled, starting first with a very slow charge of 0.02 mA/cm^2 for a total applied load Q_C of 600 mC/cm^2 , followed then by a normal discharge of -0.6 mA/cm^2 . The resulting galvanostatic curves are gathered in Fig. 5A (solid lines). For a comparative purpose, the first discharge curves previously obtained at $\text{Mn}_3\text{O}_4@\text{CNF}$ electrodes without any charging step (dashed lines) are also shown in Fig. 5. Electrodes subjected to the initial slow charging step show a systematic and almost identical increase in Q_d discharge capacity (by *ca.* 350 mC/cm^2), almost twice that of those subjected to a direct discharge. This increase in capacity suggests that the spinel Mn_3O_4 is electrochemically oxidized during the slow charging step, and thus that a certain amount of the Mn^{II} or Mn^{III} ions in the Mn_3O_4 lattice are electrochemically oxidized into either Mn^{III} or Mn^{IV} . This forces the crystalline structure to reorganize in order to accommodate changes in the Mn oxidation state, which is a very slow process, as confirmed by the particularly slow rate required for this electrochemical activation (an increase in the charging rate was observed to lead in an insignificant gain in the discharge capacity – see Fig S12). Note that this electro-oxidative activation process is characterized by a coulombic efficiency of $\sim 60\%$ (deduced from the ratio between the activation charge – 600

mC/cm^2 – and the gain in discharge – *ca.* $350 \text{ mC}/\text{cm}^2$). This low *CE* value attests to a competitive irreversible faradaic process upon charge that we supposed to be related to the oxygen evolution reaction (OER) given the reported OER catalytic activity reported for nanosized Mn_3O_4 .⁷⁶

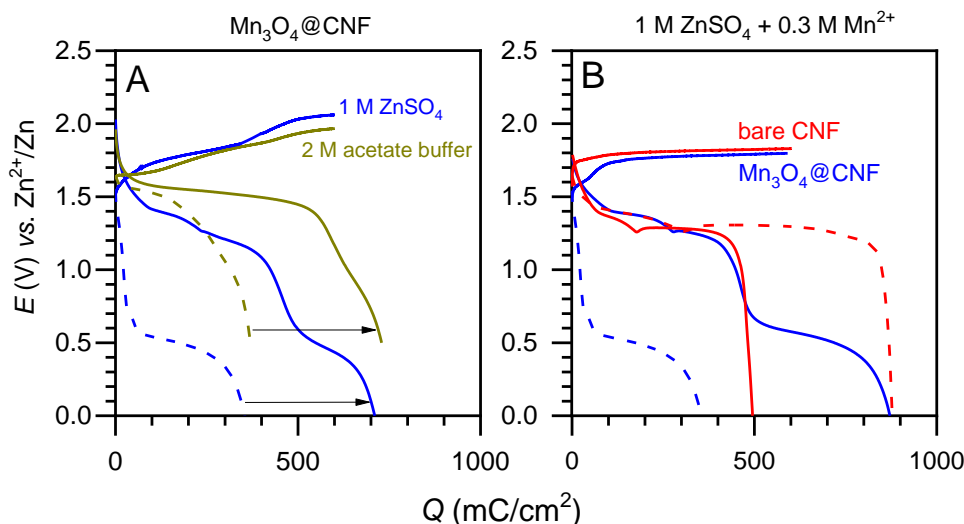


Fig. 5. (A) (plain lines) Charge-discharge curves recorded at spinel Mn_3O_4 @CNF electrodes in a (blue) 1 M ZnSO_4 (pH 4.2) and (dark yellow) 2 M acetate buffer (pH 4.7). (B) Charge-discharge curves recorded in a 1 M ZnSO_4 + 0.3 M Mn^{2+} electrolyte (pH 4.4) at a (blue) spinel Mn_3O_4 @CNF electrode and (red) bare CNF electrode. All charges were recorded at $+0.02 \text{ mA}/\text{cm}^2$ and all discharges at $-0.6 \text{ mA}/\text{cm}^2$. For comparison, are also overlaid on the graphs (dashed lines) the first discharge curves obtained at (red) MnO_2 @CNF and (blue) Mn_3O_4 @CNF electrodes in a 1 M ZnSO_4 , and (dark yellow) a Mn_3O_4 @CNF electrode in a 2 M acetate buffer.

Ex situ XPS and XRD analyses of electrodes after charge at $0.02 \text{ mA}/\text{cm}^2$ confirm the partial oxidation of Mn_3O_4 (Fig. S13). The AOS of Mn is increased from 2.67 to 3.15, which thus allowed us from eq. 1 to predict a $Q_{\text{d,th}}$ of $685 \text{ mC}/\text{cm}^2$, a value which fully agrees with the total discharge capacities achieved in the acetate buffer and ZnSO_4 electrolytes (Fig. 5A). Also, the coexistence of a new crystalline phase can be identified and attributed to a bivalence layered Mn_5O_8 ($\text{Mn}^{\text{II}}_2\text{Mn}^{\text{IV}}_3\text{O}_8$) structure according to the JCPDS file no 96-151-4101, while the morphology of the electrode is maintained (see Fig. S13). The formation of this Mn_5O_8 phase upon charge is consistent with what has been previously reported by Hao *et al.*³⁰

The subsequent discharge curve in the ZnSO_4 electrolyte shows two successive and well-separated discharge plateaus (Fig. 5A) and confirms the coexistence of different MnO_x structures at the electrode. The second plateau, localized at *ca.* 0.5 V, is reminiscent of the discharge plateau previously obtained with the direct reduction of a Mn_3O_4 @CNF electrode

(but with a lower capacity of -36 %) (dashed plots in Fig. 5A). It can thus be attributed to the faradaic reduction of Mn_3O_4 . Concerning the first discharge plateau, its presence is intrinsically linked to the prior charge process, and it should *a priori* correspond to the electrochemical reduction of the *in-situ* generated Mn_5O_8 phase.

In the buffered acetate electrolyte, the shape of the subsequent discharge shows a single plateau centered at 1.58 V (Fig. 5A), a potential value that was observed to remain relatively independent of the charging current applied during the first charge (Fig S12). *Ex situ* XRD, XPS, and SEM analysis of the fully discharged electrodes show that the MnO_x active materials (*i.e.*, Mn_3O_4 and Mn_5O_8) have completely disappeared (Fig. S13), corroborating thus their full electrodisolution under these conditions.

We next repeated the experiments in a 1 M ZnSO_4 electrolyte containing 0.3 M Mn^{2+} (pH 4.4). During the slow charge at 0.02 mA/cm^2 , the potential was observed to rapidly stabilize to *ca.* 1.78 V (plain blue plot in Fig. 5B), leading to a highly horizontal plateau (much more horizontal than that previously recorded in the Mn^{2+} -free ZnSO_4 electrolyte – see plain blue plot in Fig. 5A). This stable charging plateau is reminiscent of MnO_2 *in-situ* electrodeposited from a Mn^{2+} electrolyte (Fig. S1).^{23,66} We have thus reproduced the experiment at a bare CNF electrode (plain red plot in Fig. 5B) in order to *in-situ* electrodeposit MnO_2 onto the CNFs from Mn^{2+} in the electrolyte. The resulting charge curve almost overlaid the one previously obtained at the Mn_3O_4 @CNF electrode, suggesting thus that the same faradic process is at work whether the CNFs are covered or not with Mn_3O_4 . FEG-SEM image of the charged Mn_3O_4 electrode (Fig. S14) shows a complete coverage of the CNFs by a deposit having a morphology quite comparable to that obtained by electrodeposition of MnO_2 from Mn^{2+} in an acetate buffer (Fig. 1B). Besides, the XRD pattern of the charged electrode (Fig. S14) displays a broad signal at $2\theta = 37^\circ$ that is characteristic of amorphous MnO_2 (*i.e.*, analogous to Fig. 1A). This allows us to conclude that charging a Mn_3O_4 @CNF electrode in an Mn^{2+} -containing electrolyte leads to an *in-situ* electrodeposition of amorphous MnO_2 on top of the Mn_3O_4 coating that already covers the CNFs. It seems that under these conditions the electrochemical oxidation of Mn_3O_4 is bypassed and that it therefore remains relatively unchanged after the charge (it was not possible to discern whether some Mn_3O_4 could be oxidized to Mn_5O_8).

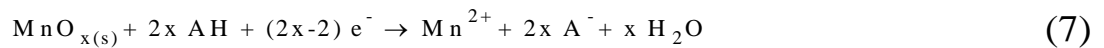
The coexistence of amorphous MnO_2 and Mn_3O_4 onto the CNFs was confirmed from the subsequent discharge at -0.6 mA/cm^2 (plain blue curve in Fig. 5B), which presents a multiphasic behavior with well-defined plateaus. The first part of the multiphasic discharge (*i.e.*, corresponding roughly to the first plateau) is close to that recorded at the bare CNF

electrode charged *in situ* (dashed red curve in Fig. 5A), so we can attribute it to the discharge of the *in-situ* electrodeposited amorphous MnO₂. The second discharge plateau is reminiscent of the one obtained during the direct discharge of the Mn₃O₄@CNF electrode, both in terms of voltage (~0.4 V) and capacity. It can therefore be attributed to the Mn₃O₄ discharge, in the same proportion as for an electrode that has not undergone oxidative activation. This further confirms that direct oxidation of Mn₃O₄ cannot occur in aqueous electrolytes containing a significant amount of Mn²⁺ ions. Finally, FEG-SEM analysis of the electrode after discharge confirms the full electrodisolution of both of the MnO_x active materials (*i.e.*, Mn₃O₄ and MnO₂), showing only the expected precipitates of zinc hydroxide (Fig. S14).

Overall, these observations demonstrate that charging a Mn₃O₄ electrode in a ZnSO₄ electrolyte containing Mn²⁺ leads primarily to *in-situ* electrodeposition of amorphous MnO₂, while the pristine Mn₃O₄ material remains largely unaffected by this electrochemical oxidation step. Accordingly, the increased capacity of the electrode resulting from the initial charge is only due to the deposition of an extra mass of active MnO₂ material. It should therefore not be confused with a true activation process relying on direct Mn₃O₄ oxidation, which can therefore only take place in the absence of Mn²⁺.

3. Conclusions

The above results clearly demonstrate that the discharge mechanism of low-valence MnO_x electrodes in aqueous electrolytes operate through a proton-coupled electrochemical dissolution of the active material, analogous to the proton-coupled electrodisolution mechanism that has been now well established for the high-valence MnO₂ electrodes. This implies that the present results refute the previously reported mechanisms of reversible insertion/intercalation of multivalent cations such as Zn²⁺ or Al³⁺, as well as the insertion/co-insertion of monovalent cations such as H⁺ or NH₄⁺ in low-valence MnO_x crystalline structures (see Table S1, which summarizes the different mechanisms so far proposed). This also reveals that whatever the oxidation state of Mn (2 < AOS of Mn ≤ 4) in the MnO_x material and the degree of crystallinity of the structure (including thus the spinel Mn₃O₄), the discharge mechanism follows a common proton-coupled electrodisolution reaction, in which the protons essential to the electrochemical reaction are recruited from the most acidic proton donors available in the aqueous electrolyte as follow:



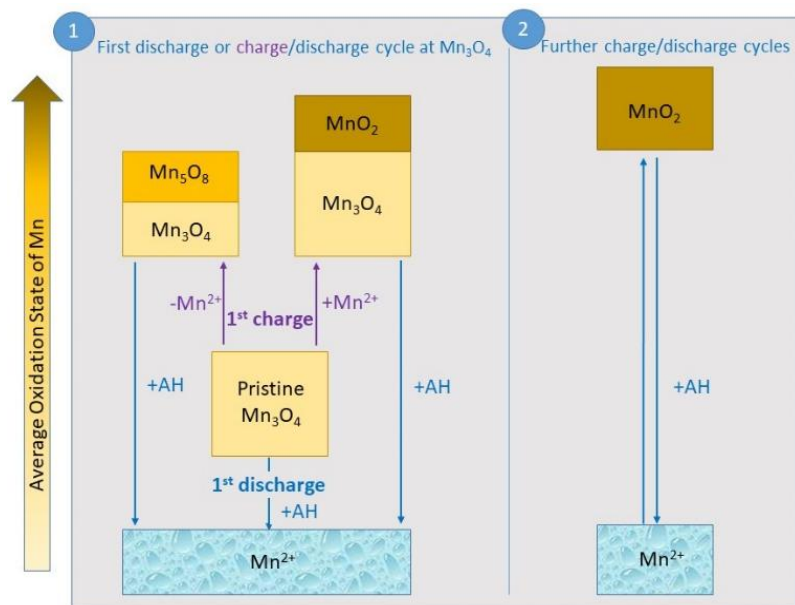
where x ($1 < x \leq 2$) represents the average number of oxygen atoms per Mn center in the structure (for instance, $x = 4/3$ for Mn_3O_4), $2x$ is given by the AOS number, and $(2x-2)$ corresponds to the average number of e^- transferred per Mn center (for instance, $0.67 e^-$ for Mn_3O_4 with $x = 4/3$).

We also revealed several key features of Mn_3O_4 reactivity in aqueous electrolytes, notably:

- the significant dismutation of Mn_3O_4 in acidic electrolytes, thereby leading to its *in-situ* chemical conversion into MnO_2 ;
- the much slower electrodisolution rate of Mn_3O_4 than amorphous MnO_2 , especially when working in the presence of a Zn^{2+} -based mild aqueous electrolyte, which is consistent with the high stability of the 3D spinel structure in the absence of dismutation;
- the slow electrochemical phase transformation of Mn_3O_4 into a Mn_5O_8 phase upon charging in a Mn^{2+} -free electrolyte, since otherwise the latter is bypassed by the electrodeposition of an amorphous MnO_2 phase on top of Mn_3O_4 .

It is also here crucial to emphasize that reaction 7 is irreversible for all crystalline MnO_x structures, because after the first discharge leading to full electrodisolution of the starting material, the pristine structure of MnO_x cannot be regenerated by simple electrodeposition. Indeed, in the subsequent charge/discharge cycles this is an amorphous film of MnO_2 that is reversibly electrodeposited from the pre-added and/or released Mn^{2+} ions in the electrolyte (see in SI the note on the cyclability of $\text{Mn}_3\text{O}_4@\text{CNF}$ in a mild buffered electrolyte). However, it is important to note that for this process to take place, there must be a high enough concentration of a weak acid in the electrolyte, which is the case when working in the presence of a few molars Zn^{2+} -based electrolyte, in which the weak acid $\text{Zn}[\text{H}_2\text{O}]_6^{2+}$ species can act as a proton donor to trigger reaction 7. This mechanism of irreversible transformation of any MnO_x phase into soluble Mn^{2+} followed by reversible electrodeposition of an amorphous MnO_2 phase from Mn^{2+} in solution also allows to understand the activation mechanism underlying the conversion of Mn_3O_4 to MnO_2 reported or suggested in many studies.^{30,31,36,37,40,42,43} Moreover, with such a conversion mechanism it is definitely no more relevant to analyze the MnO_x cathode performance through normalization with the initial mass of the cathode's active material.

The present study finally provides a better overview and comprehension of the relatively complex electrochemical reactivity of low-valence MnO_x cathodes in mild aqueous electrolytes, a complexity that is summarized in Scheme 1.



Scheme 1. Schematic description of the overall electrochemical reactivity of Mn_3O_4 (including thus its different phase transformations) in a mild aqueous electrolyte containing a proton donor AH and Mn^{2+} ions.

Supporting Information

Supporting Information is available from the Wiley Online Library or from the author.

Acknowledgements

David Montero is gratefully acknowledged for helping in SEM & EDS experiments. SEM & EDS were funded by Sorbonne Université, CNRS and Région Ile de France, and are part of FCMat, The Federation of Chemistry and Materials of Paris-Center. The authors also gratefully acknowledge financial support from the French National Agency (ANR AqReBat project).

Notes and References

[‡]The peak in dQ/dV vs. potential plot occurs at a potential nearly identical to half-discharge potential E_d of the discharge plateau. Therefore, any one of them can be considered as discharge plateau potential for analysis.

[&]Note that in the absence of the preadded Mn^{2+} in the buffered electrolyte, $a_{\text{Mn}^{2+}}$ is very low and governed by the amount of Mn^{2+} *in situ* released during the discharge of the electrode. This low $a_{\text{Mn}^{2+}}$ is thus expected to lead in a small up-shift of the discharge plateau potential according to eq. 4.¹¹

[§]Note that the release of Mn^{2+} by dismutation of Mn_3O_4 does not affect the total gravimetric capacity of the manganese oxide film for the reason that the AOS of Mn in the remaining solid electrode material is concomitantly increased during this process (eq. 6).

^ϕ Note that in the absence of zinc salt in the buffered electrolyte, the charge voltage in our two-electrode cell configuration is rather defined vs. H^+/H_2 at the zinc anode and can thus not be directly compared to that recorded in the 1 M ZnSO_4 electrolyte.

References

- [1] V. Mathew, B. Sambandam, S. Kim, S. Kim, S. Park, S. Lee, M. H. Alfaruqi, V. Soundharrajan, S. Islam, D. Y. Putro, J.-Y. Hwang, Y.-K. Sun, J. Kim, *ACS Energy Lett.* **2020**, *5*, 2376.
- [2] G. Fang, J. Zhou, A. Pan, S. Liang, *ACS Energy Lett.* **2018**, *3*, 2480.
- [3] L. Xiaoyu, Y. Jin, W. Kai, J. Yong, L. Yuyu, Z. Bing, L. Wenrong, Z. Jiujun, *Nanotechnology*, **2020**, *31*, 122001.
- [4] H. Pan, Y. Shao, P. Yan, Y. Cheng, K. S. Han, Z. Nie, C. Wang, J. Yang, X. Li, P. Bhattacharya, K. T. Mueller, J. Liu, *Nat. Energy* **2016**, *1*, 16039.
- [5] A. Biswal, B. Chandra Tripathy, K. Sanjay, T. Subbaiah, M. Minakshi, *RSC Adv.* **2015**, *5*, 58255.
- [6] C. M. Julien, A. Mauger, *Nanomaterials* **2017**, *7*, 396.
- [7] M. Wang, X. Zheng, X. Zhang, D. Chao, S.-Z. Qiao, H. N. Alshareef, Y. Cui, W. Chen, *Adv. Energy Mater.* **2021**, *11*, 2002904.
- [8] R. Demir-Cakan, M. R. Palacin, L. Croguennec, *J. Mater. Chem. A* **2019**, *7*, 20519.
- [9] Y. Gao, H. Yang, Y. Bai, C. Wu, *J. Mater. Chem. A* **2021**, *9*, 11472.
- [10] L. Xu, N. Xu, C. Yan, W. He, X. Wu, G. Diao, M. Chen, *J. Electroanal. Chem.* **2021**, 888, 115196.
- [11] M. Mateos, N. Makivic, Y.-S. Kim, B. Limoges, V. Balland, *Adv. Energy Mater.* **2020**, *10*, 2000332.
- [12] C. Xie, T. Li, C. Deng, Y. Song, H. Zhang, X. Li, *Energy Environ. Sci.* **2020**, *13*, 135.
- [13] D. Wu, L. M. Housel, S. J. Kim, N. Sadique, C. D. Quilty, L. Wu, R. Tapper, S. L. Nicholas, S. Ehrlich, Y. Zhu, A. C. Marschilok, E. S. Takeuchi, D. C. Bock, K. J. Takeuchi, *Energy Environ. Sci.* **2020**, *13*, 4322.
- [14] X. Zeng, J. Liu, J. Mao, J. Hao, Z. Wang, S. Zhou, C. D. Ling, Z. Guo, *Adv. Energy Mater.* **2020**, *10*, 1904163.
- [15] M. Mateos, K. D. Harris, B. Limoges, V. Balland, *ACS Appl. Energy Mater.* **2020**, *3*, 7610.
- [16] V. Balland, M. Mateos, A. Singh, K. D. Harris, C. Laberty-Robert, B. Limoges, *Small* **2021**, *17*, 2101515.
- [17] J. Yang, J. Cao, Y. Peng, W. Yang, S. Barg, Z. Liu, I. A. Kinloch, M. A. Bissett, R. A. W. Dryfe, *ChemSusChem* **2020**, *13*, 4103.
- [18] X. Guo, J. Zhou, C. Bai, X. Li, G. Fang, S. Liang, *Mater. Today Energy* **2020**, *16*, 100396.
- [19] S. J. Kim, D. Wu, N. Sadique, C. D. Quilty, L. Wu, A. C. Marschilok, K. J. Takeuchi, E. S. Takeuchi, Y. Zhu, *Small* **2020**, *16*, 2005406.
- [20] J. Lei, Y. Yao, Z. Wang, Y.-C. Lu, *Energy Environ. Sci.* **2021**, *14*, 4418.
- [21] W. Liu, X. Zhang, Y. Huang, B. Jiang, Z. Chang, C. Xu, F. Kang, *J. Energy Chem.* **2021**, *56*, 365.
- [22] I. Stoševski, A. Bonakdarpour, B. Fang, P. Lo, D. P. Wilkinson, *Electrochim. Acta* **2021**, *390*, 138852.
- [23] G. Li, W. Chen, H. Zhang, Y. Gong, F. Shi, J. Wang, R. Zhang, G. Chen, Y. Jin, T. Wu, Z. Tang, Y. Cui, *Adv. Energy Mater.* **2020**, *10*, 1902085.
- [24] O. Fitz, C. Bischoff, M. Bauer, H. Gentischer, K. P. Birke, H. M. Henning, D. Biro, *ChemElectroChem* **2021**, *8*, 3553.
- [25] U. Siamionau, Y. Aniskevich, A. Mazanik, O. Kokits, G. Ragoisha, J. H. Jo, S.-T. Myung, E. Streltsov, *J. Power Sources* **2022**, 523, 231023.
- [26] D. Zhang, J. Cao, X. Zhang, N. Insin, S. Wang, J. Han, Y. Zhao, J. Qin, Y. Huang, *Adv. Funct. Mater.* **2021**, *31*, 2009412.
- [27] N. Liu, X. Wu, Y. Yin, A. Chen, C. Zhao, Z. Guo, L. Fan, N. Zhang, *ACS Appl. Mater. Interfaces* **2020**, *12*, 28199.
- [28] W. Li, X. Gao, Z. Chen, R. Guo, G. Zou, H. Hou, W. Deng, X. Ji, J. Zhao, *Chem. Eng. J.* **2020**, *402*, 125509.
- [29] B. Jiang, C. Xu, C. Wu, L. Dong, J. Li, F. Kang, *Electrochim. Acta* **2017**, *229*, 422.
- [30] J. Hao, J. Mou, J. Zhang, L. Dong, W. Liu, C. Xu, F. Kang, *Electrochim. Acta* **2018**, *259*, 170.
- [31] L. Wang, X. Cao, L. Xu, J. Chen, J. Zheng, *ACS Sustainable Chem. Eng.* **2018**, *6*, 16055.

- [32] C. Zhu, G. Fang, J. Zhou, J. Guo, Z. Wang, C. Wang, J. Li, Y. Tang, S. Liang, *J. Mater. Chem. A* **2018**, *6*, 9677.
- [33] C. Wu, S. Gu, Q. Zhang, Y. Bai, M. Li, Y. Yuan, H. Wang, X. Liu, Y. Yuan, N. Zhu, F. Wu, H. Li, L. Gu, J. Lu, *Nat. Commun.* **2019**, *10*, 73.
- [34] H. Chen, W. Zhou, D. Zhu, Z. Liu, Z. Feng, J. Li, Y. Chen, *J. Alloys Compd.* **2020**, *813*, 151812.
- [35] J. Ji, H. Wan, B. Zhang, C. Wang, Y. Gan, Q. Tan, N. Wang, J. Yao, Z. Zheng, P. Liang, J. Zhang, H. Wang, L. Tao, Y. Wang, D. Chao, H. Wang, *Adv. Energy Mater.* **2020**, *11*, 2003203.
- [36] I. Stoševski, A. Bonakdarpour, B. Fang, S. T. Voon, D. P. Wilkinson, *Int. J. Energy Res.* **2020**, *45*, 220.
- [37] Q. Tan, X. Li, B. Zhang, X. Chen, Y. Tian, H. Wan, L. Zhang, L. Miao, C. Wang, Y. Gan, J. Jiang, Y. Wang, H. Wang, *Adv. Energy Mater.* **2020**, *10*, 2001050.
- [38] Y. Ma, Y. Ma, T. Diemant, K. Cao, X. Liu, U. Kaiser, R. J. Behm, A. Varzi, S. Passerini, *Adv. Energy Mater.* **2021**, *11*, 2100962.
- [39] G. Ren, Z. Luo, Y. Duan, X. Liu, Z. Yuan, F. Cai, *J. Alloys Compd.* **2022**, *898*, 162747.
- [40] J. Long, Z. Yang, F. Yang, J. Cuan, J. Wu, *Electrochim. Acta* **2020**, *344*, 136155.
- [41] M. B. Sassin, M. E. Helms, J. F. Parker, C. N. Chervin, R. H. DeBlock, J. S. Ko, D. R. Rolison, J. W. Long, *Mater. Adv.* **2021**, *2*, 2730.
- [42] T.-B. Song, Z.-H. Huang, X.-Q. Niu, X.-R. Zhang, J.-S. Wei, H.-M. Xiong, *ChemSusChem* **2022**, *15*, e202102390.
- [43] Z. Huang, Y. Duan, Q. Jing, M. Sun, B. Tang, S. Shi, *J. Alloys Compd.* **2021**, *864*, 158316.
- [44] A. Singh, A. Rafie, V. Kalra, *Sustainable Energy Fuels* **2019**, *3*, 2788.
- [45] A. Singh, O. Sel, H. Perrot, V. Balland, B. Limoges, C. Laberty-Robert, *J. Mater. Chem. A* **2021**, *9*, 1500.
- [46] A. Gupta, S. R. Dhakate, P. Pal, A. Dey, P. K. Iyer, D. K. Singh, *Diamond Relat. Mater.* **2017**, *78*, 31.
- [47] J.-K. Chang, W.-T. Tsai, *J. Electrochem. Soc.* **2003**, *150*, A1333.
- [48] M. Huynh, D. K. Bediako, Y. Liu, D. G. Nocera, *J. Phys. Chem. C* **2014**, *118*, 17142.
- [49] D. Chao, W. Zhou, C. Ye, Q. Zhang, Y. Chen, L. Gu, K. Davey, S.-Z. Qiao, *Angew. Chem. Int. Ed.* **2019**, *58*, 7823.
- [50] W. Yan, T. Ayvazian, J. Kim, Y. Liu, K. C. Donovan, W. Xing, Y. Yang, J. C. Hemminger, R. M. Penner, *ACS Nano* **2011**, *5*, 8275.
- [51] S. Upadhyay, K. Parekh, B. Pandey, *J. Alloys Compd.* **2016**, *678*, 478.
- [52] Y. Fu, Q. Wei, G. Zhang, X. Wang, J. Zhang, Y. Hu, D. Wang, L. Zuin, T. Zhou, Y. Wu, S. Sun, *Adv. Energy Mater.* **2018**, *8*, 1801445.
- [53] L. Chen, Y. F. Yuan, P. F. Du, S. M. Yin, M. Zhu, S. Y. Guo, *Nanotechnology* **2021**, *32*, 405403.
- [54] J. Joseph, J. Nerkar, C. Tang, A. Du, A. P. O'Mullane, K. Ostrikov, *ChemSusChem* **2019**, *12*, 3753.
- [55] C. Yan, C. Lv, L. Wang, W. Cui, L. Zhang, K. N. Dinh, H. Tan, C. Wu, T. Wu, Y. Ren, J. Chen, Z. Liu, M. Srinivasan, X. Rui, Q. Yan, G. Yu, *J. Am. Chem. Soc.* **2020**, *142*, 15295.
- [56] R. Li, C. Xu, X. Wu, J. Zhang, X. Yuan, F. Wang, Q. Yao, M. Sadeeq Balogun, Z. Lu, J. Deng, *Energy Storage Mater.* **2022**, *53*, 514.
- [57] S. Nandi, S. K. Das, *Phys. Chem. Chem. Phys.* **2021**, *23*, 19150.
- [58] C. F. Bischoff, O. S. Fitz, J. Burns, M. Bauer, H. Gentischer, K. P. Birke, H.-M. Henning, D. Biro, *J. Electrochem. Soc.* **2020**, *167*, 020545.
- [59] Y. S. Kim, K. D. Harris, B. Limoges, V. Balland, *Chem. Sci.* **2019**, *10*, 8752.
- [60] S. J. Hawkes, *J. Chem. Edu.*, **1996**, *73*, 516.
- [61] M. Li, Q. He, Z. Li, Q. Li, Y. Zhang, J. Meng, X. Liu, S. Li, B. Wu, L. Chen, Z. Liu, W. Luo, C. Han, L. Mai, *Adv. Energy Mater.* **2019**, *9*, 1901469.
- [62] T. Shoji, T. Yamamoto, *J. Electroanal. Chem.* **1993**, *362*, 153.
- [63] P. Oberholzer, E. Tervoort, A. Bouzid, A. Pasquarello, D. Kundu, *ACS Appl. Mater. Interfaces* **2019**, *11*, 674.
- [64] B. Lee, H. R. Seo, H. R. Lee, C. S. Yoon, J. H. Kim, K. Y. Chung, B. W. Cho, S. H. Oh, *ChemSusChem* **2016**, *9*, 2948.
- [65] Z. You, W. Hua, N. Li, H. Liu, J.-G. Wang, *Chin. Chem. Lett.* **2023**, *34*, 107525.
- [66] I. Aguilar, P. Lemaire, N. Ayouni, E. Bendadesse, A. V. Morozov, O. Sel, V. Balland, B. Limoges, A. M. Abakumov, E. Raymundo-Piñero, A. Slodczyk, A. Canizarès, D. Larcher, J.-M. Tarascon, *Energy Storage Mater.* **2022**, *53*, 238.
- [67] Q. Zhao, A. Song, W. Zhao, R. Qin, S. Ding, X. Chen, Y. Song, L. Yang, H. Lin, S. Li, F. Pan, *Angew. Chem. Int. Ed.* **2021**, *60*, 4169.
- [68] Y. Zuo, P. Liu, L. Ling, M. Tian, Z. Wang, H. Tian, T. Meng, X. Sun, S. Cai, *ACS Appl. Mater. Interfaces* **2022**, *14*, 26653.
- [69] X. Gao, H. Wu, W. Li, Y. Tian, Y. Zhang, H. Wu, L. Yang, G. Zou, H. Hou, X. Ji, *Small* **2020**, *16*, 1905842.
- [70] K. J. Powell, P. L. Brown, R. H. Byrne, T. Gajda, G. Hefter, A.-K. Leuz, S. Sjöberg, H. Wanner, *Pure Appl. Chem.* **2013**, *85*, 2249.
- [71] A. N. Chowdhury, M. S. Azam, M. Aktaruzzaman, A. Rahim, *J. Hazard Mater.* **2009**, *172*, 1229.

- [72] A. J. Bard, R. Parsons, J. Jordan, *CRC Press* **1985**.
- [73] I. V. Artamonova, I. G. Gorichev, E. B. Godunov, *Engineering* **2013**, 05, 714.
- [74] K. V. Sankar, D. Kalpana, R. K. Selvan, *J. Appl. Electrochem.* **2012**, 42, 463.
- [75] N. Wang, H. Wan, J. Duan, X. Wang, L. Tao, J. Zhang, H. Wang, *Mater. Today Adv.* **2021**, 11, 100149.
- [76] K. H. Cho, H. Seo, S. Park, Y. H. Lee, M. Y. Lee, N. H. Cho, K. T. Nam, *Adv. Funct. Mater.* **2020**, 30, 1910424.

Supporting Information

Experimental Section

i. Chemicals and electrolytes

N, N-dimethylformamide (DMF), and glacial acetic acid were purchased from CARLO ERBA Reagents. Polyacrylonitrile (PAN, Average M_w 150000), potassium acetate (BioUltra, $\geq 99.0\%$), potassium chloride (BioXtra $\geq 99.0\%$), and manganese (II) chloride ($\geq 99\%$) were purchased from Sigma Aldrich.

ii. Preparation of cathodes and their characterizations

Free-standing 3D CNF substrates were prepared by electrospinning using a previously reported protocol.^{S1-S2} The amorphous MnO_2 thin films deposited on disk-shaped CNF substrates (10 mm diameter, 0.785 cm^2 , $1.50 \pm 0.10\text{ mg}_{CNF}/\text{cm}^2$) were prepared in a 2-electrode Swagelok cell by galvanostatic electrodeposition at $+1\text{ mA}/\text{cm}^2$ in a 2 M acetate buffer containing 0.3 M $MnCl_2$ (pH 4.70). After a total charge (Q_T) of $1\text{ C}/\text{cm}^2$ was passed, the resulting amorphous MnO_2 -coated CNF electrodes (*i.e.*, amorphous $MnO_2@CNF$) were washed thoroughly with de-ionized (DI) water to ensure complete removal of the residual electrolyte and then dried at room temperature overnight. To generate the $Mn_3O_4@CNF$ electrodes, the samples were heated in a tube furnace at different temperatures (300, 400, and 500°C) for 1 h under steady-state Ar flow. For the MnO_x/FTO samples, an identical route was followed. However, electrodeposition was performed for a total charge (Q_T) = 20 or 50 mC/cm^2 at $+0.1\text{ mA}/\text{cm}^2$ vs. Ag/AgCl (sat. KCl) using a standard 3-electrode cell.

Microstructural/morphological features were investigated using field emission gun scanning electron microscopy (FEG-SEM) (Zeiss, Supra 55) equipped with an energy dispersive spectrometer (EDS). High-resolution transmission electron microscopy (HRTEM) analysis with lattice spacing, selected area electron diffraction (SAED), and line-scanning elemental mapping (C, Mn, O) was performed on the JEOL JEM-2100Plus microscope with an acceleration voltage of 200 kV, EDS Analyzer (PGT) and Beam scanning system (STEM). Samples were prepared by sonication of a tiny amount of the material (5-10 $\mu\text{g}/\text{ml}$) in ethanol for 30 minutes and thereafter by pipetting 3-5 μL of the dispersion onto carbon-coated TEM copper grids for analysis. The ImageJ software was used to estimate the lattice spacing from the HRTEM image. X-ray diffraction (XRD) measurements were performed under ambient conditions using an X-ray diffractometer (Phillips PANanalytical X'Pert Pro) with Cu K_α radiation ($\lambda = 1.54184\text{ \AA}$) source. The mean size of the ordered (crystalline) domain (τ) was calculated from the Scherrer formula according to:

$$\tau = K\lambda/\beta\cos\theta \quad (S1)$$

where $\lambda = 1.54184 \text{ \AA}$, 2θ = peak position, β = full-width half maxima and K is the shape factor taken as 1.

Core-level X-ray photoelectron spectroscopy (XPS) spectra were collected using a VG ESCALAB 250i-XL spectrometer equipped with a monochromatic Al K_{α} excitation source. XPS spectra were charge-corrected to the binding energy of the C 1s peak position (284.6 eV). The fitting of the core-level spectra was done using CasaXPS software and with the Shirley background. The average oxidation state of Mn was estimated from the Mn 3s peak separation ΔE (eV), using the following equation:^{S3}

$$\text{AOS} = 8.95 - 1.13 \times \Delta E \text{ (eV)} \quad (S2)$$

Accordingly, the MnO_2 load on the CNF was calculated from:

$$m_{\text{MnO}_2} = Q_T \times \text{MW}_{\text{MnO}_2} / nF \quad (S3)$$

where MW_{MnO_2} is 87 g/mol, F is 96 485 C/mol, and Q_T is 1 C/cm².

The X-ray fluorescence measurements are performed on an Epsilon 3XL energy dispersive spectrometer (@Malvern-Panalytical). Two different conditions are chosen to quantify Mn and Sn: for Mn 20kV - 15 μA in air, while for Sn 50kV - 6 μA in air. Calibration curves are established using standard solutions with a concentration of 1 g/L and deposited on polycarbonate membrane for different volume and consequently mass, with an agreement factor greater than 0.995 for each element. When the samples are thin, it is considered that the matrix effects are negligible and that the intensity measured under each peak is directly proportional to the mass. As for the samples during measurements, they are positioned on thin prolene membranes (very transparent to X-rays).

iii. Electrochemical testing:

Galvanostatic charge–discharge (GCD) analyses of cathodes were performed by biologic potentiostat interfaced with EC lab software. Swagelok T cells (ID 12 mm) were used for 2-electrode (vs. Zn/Zn^{2+}) measurements for self-standing CNF/ MnO_x samples with 800 μL of electrolyte. For the FTO/ MnO_x electrodes, a standard 3-electrode cell with 8-10 mL of electrolyte was used for recording the first galvanostatic discharge (vs. Ag/AgCl) in various buffered aqueous solutions. This 3-electrode cell configuration was used for these measurements because the pressure manually applied during customized 2-electrode Swagelok cell assembly (without spring) could slightly change the ‘IR’ drop and thus influence the discharge plateau potential. Moreover, the use of a true reference electrode allows accurate measurement of the discharge potential, for better reproducibility of the cell

assembly (and thus ohmic drop) as well as accurate monitoring of the cathode potential (vs. Ag/AgCl reference electrode).^{S4} For the post-mortem studies, electrodes were removed from the cell, washed thoroughly with de-ionized water to remove the residual electrolyte, and then dried at room temperature overnight before analysis.

Supplementary Figures

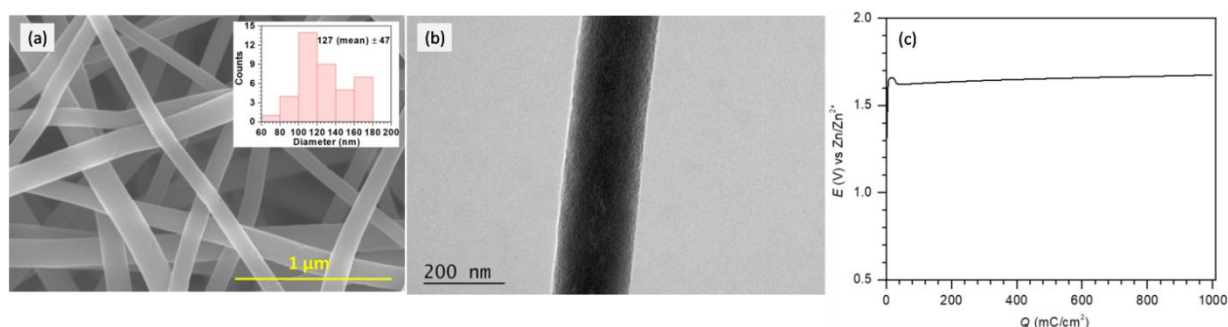


Fig. S1. (a-b) FEG–SEM and HRTEM images of carbon nanofibers (CNFs) and distribution of fiber diameter (inset to (a)) estimated using ImageJ software. (c) Representative galvanostatic trace recorded during the electrodeposition of MnO_2 ($Q_T = 1 \text{ C/cm}^2$ at $+1 \text{ mA/cm}^2$) at a CNF disk electrode (10 mm diameter, 0.785 cm^2 , $1.50 \pm 0.10 \text{ mg}_{\text{CNF}}/\text{cm}^2$) from a 2 M acetate buffer containing 0.3 M MnCl_2 (pH 4.70). A two-electrode Swagelok cell with a Zn foil was used.

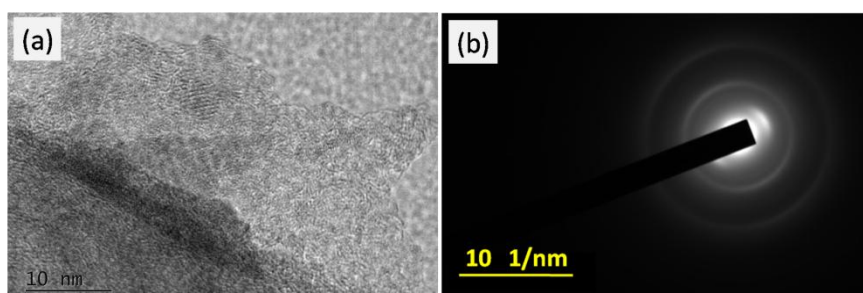


Fig. S2. (a) Dark-field scanning transmission electron microscopy (STEM) image, and (b) SAED pattern for the as-deposited amorphous MnO_2 on a CNF sample.

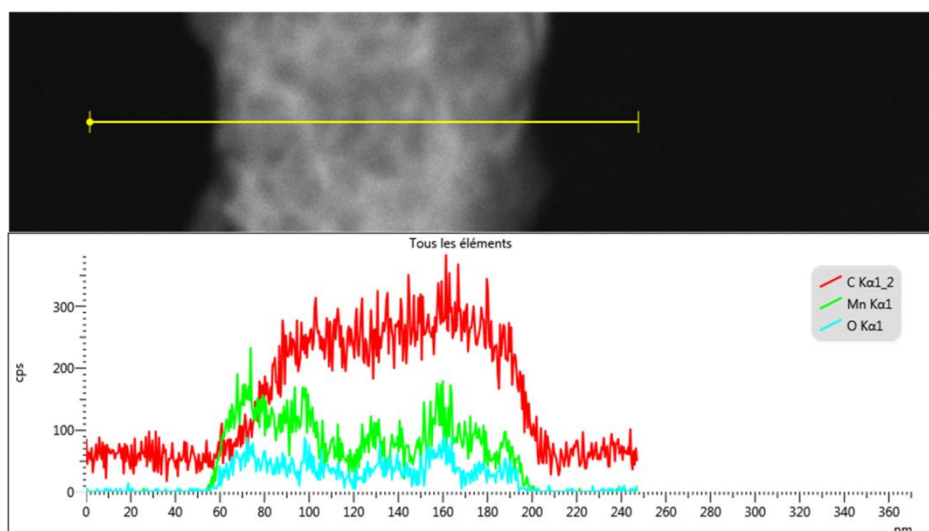


Fig. S3. The line-scanning elemental mapping (C, Mn, O) performed during the HRTEM analysis of a CNF coated with the electrodeposited amorphous MnO_2 film.

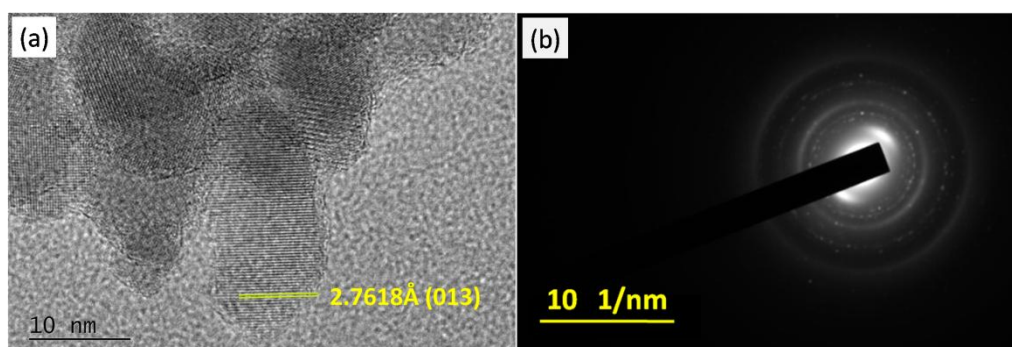


Fig. S4. (a) Dark-field scanning transmission electron microscopy (STEM) image and (b) SAED pattern of the spinel Mn_3O_4 material formed on a CNF sample.

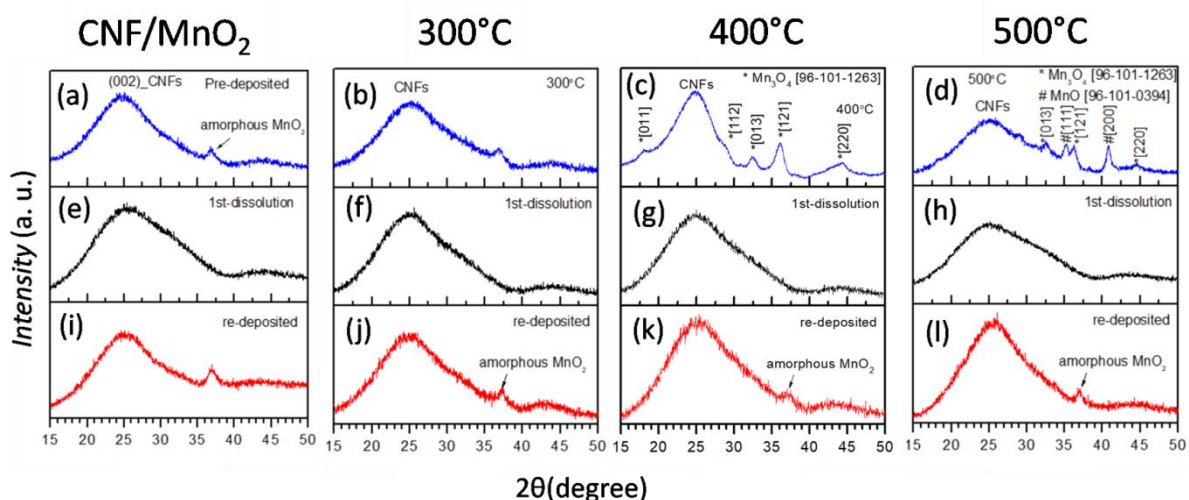


Fig. S5. XRD patterns recorded for the different MnO_x@CNF electrodes (the annealing temperatures used for the preparation of the electrode are indicated on top of the graphs) at three different stages: (a-d) for the as-prepared materials, (e-h) after completion of the first discharge and (i-l) then subsequent charge (redeposition) of the MnO_x material in an aqueous Al(OTf)₃ solution containing 0.3 M Mn²⁺ (pH 1.7).

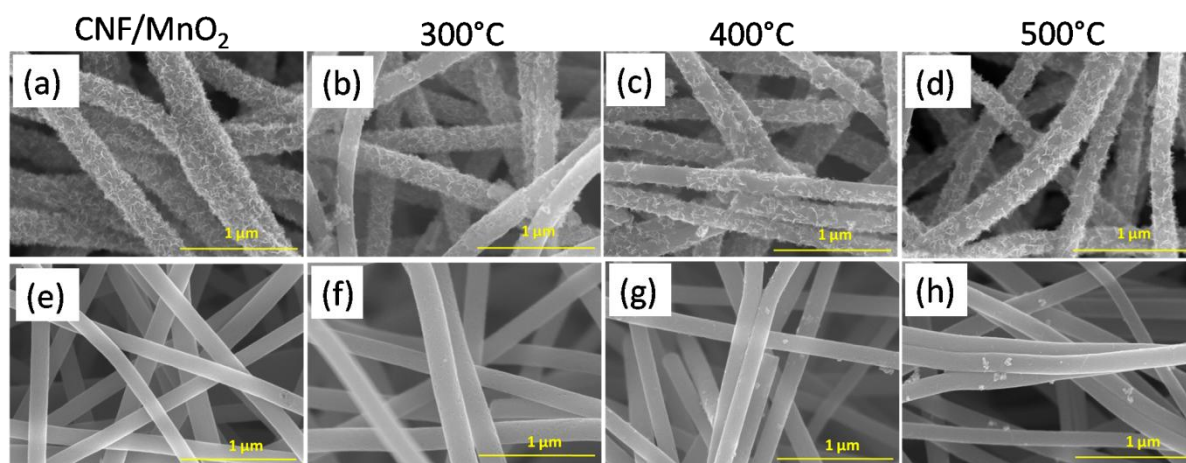


Fig. S6. (a-d) FEG-SEM images recorded for the different as-prepared MnO_x@CNF electrodes (the annealing temperatures are indicated on top of the graphs) and (e-h) after completion of the first discharge in an aqueous Al(OTf)₃ solution containing 0.3 M Mn²⁺ (pH 1.7).

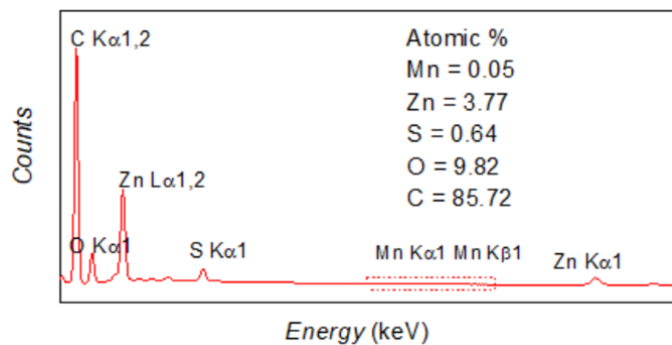


Fig. S7. Post-mortem energy dispersive spectroscopy (EDS) spectra for the fully discharged $\text{Mn}_3\text{O}_4@\text{CNF}$ electrode at -0.6 mA/cm^2 in a 1 M ZnSO_4 aqueous electrolyte (pH 4.2).

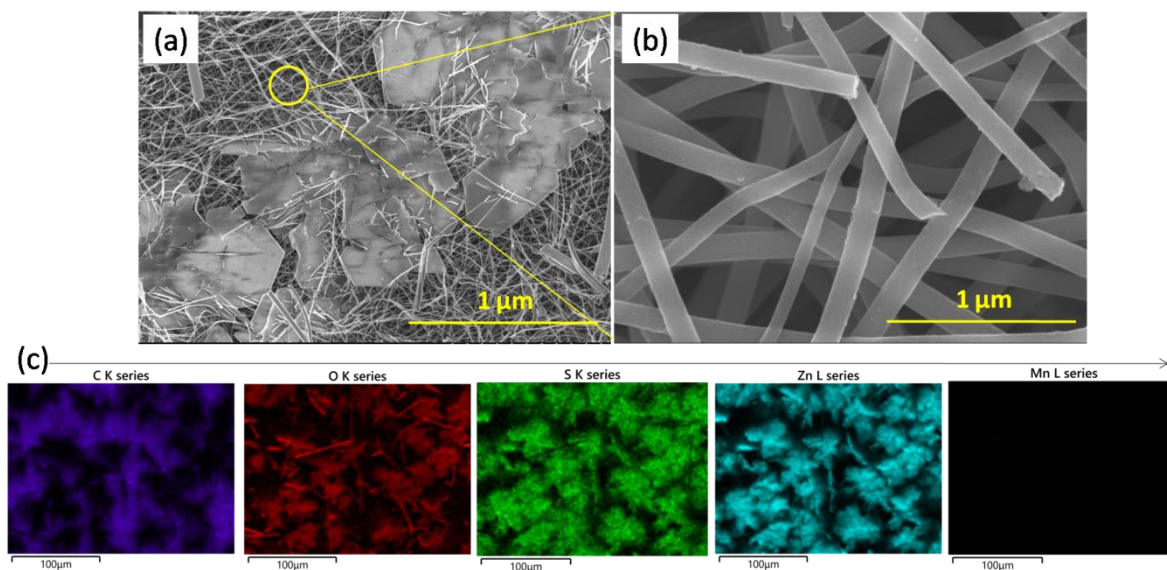


Fig. S8. Post-mortem (a-b) FEG-SEM images and (c) elemental (C, O, S, Zn, Mn) maps of a fully discharged $\text{Mn}_3\text{O}_4@\text{CNF}$ electrode (at a slow rate of -0.012 mA/cm^2) in a 1 M ZnSO_4 aqueous electrolyte (pH 4.2).

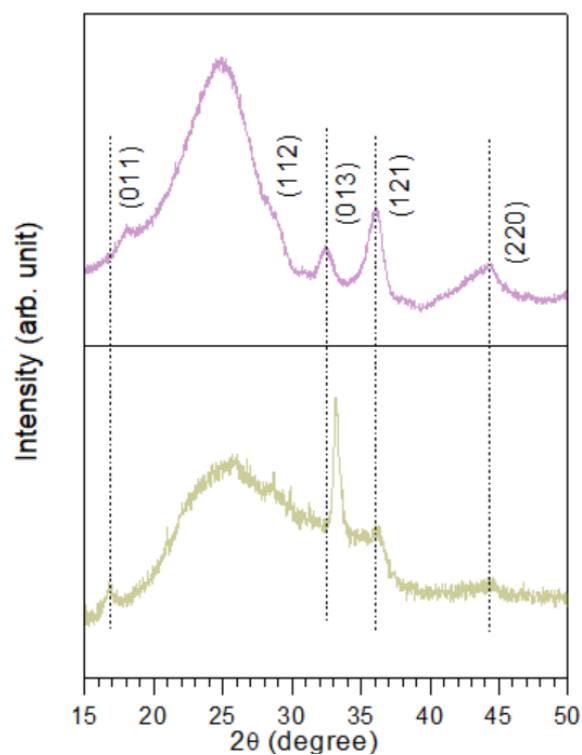


Fig. S9. XRD patterns of a pristine (top) and fully discharged (bottom) $\text{Mn}_3\text{O}_4@\text{CNF}$ electrode (discharge rate: -0.012 mA/cm^2) in a 1 M ZnSO_4 aqueous electrolyte (pH 4.2).

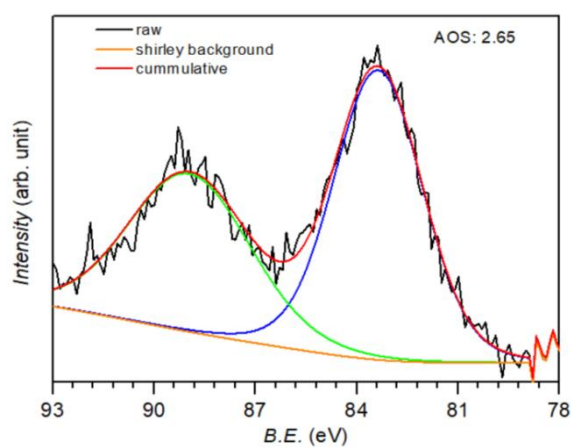


Fig. S10. Core-level Mn 3s XPS spectra of a $\text{MnO}_2@\text{FTO}$ electrode annealed at 400°C .

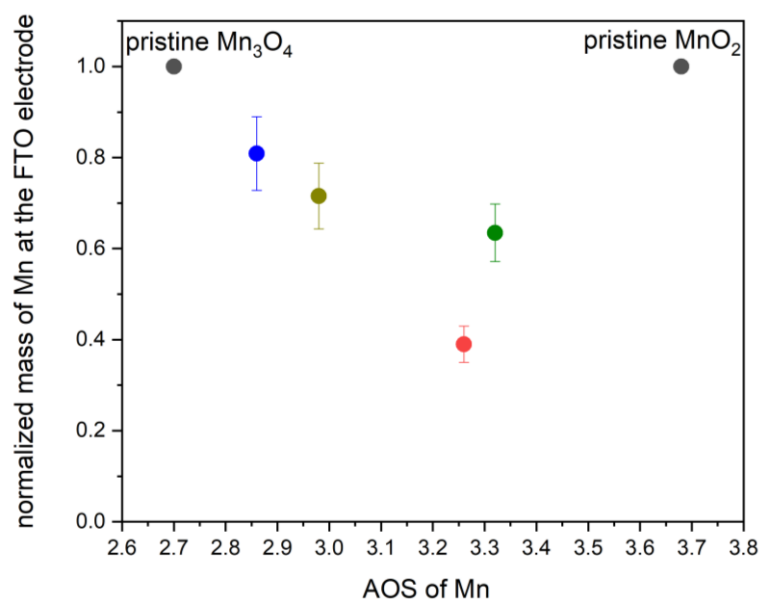


Fig. S11. Residual mass of Mn and AOS of Mn obtained for Mn_3O_4 @FTO electrodes after 15 min soaking in electrolytes of various composition and pH: (blue) 1 M ZnSO_4 (pH ~5), (dark yellow) 1 M acetate buffer containing 0.3 M Mn^{2+} (pH 4.5), (olive) 1.3 M $\text{Al}(\text{OTf})_3$ containing 0.3 M Mn^{2+} (pH 1.96), and (red) 1.5 M HCl (pH 0).

Comment on Figure S11. Briefly, FTO electrodes were loaded with amorphous MnO_2 up to 50 mC/cm^2 and the absorbance of the electrodes were then measured to estimate the actual mass of deposited MnO_2 according to a previously published protocol.^{S4} The electrodes were next heated up to 400°C to be converted to spinel Mn_3O_4 and further soaked for 15 minutes in the aqueous electrolyte. After carefully rinsing with milliQ water, the electrodes were dried in air and analyzed by XPS as well as XRF. The AOS of Mn was deduced from the Mn 3s peak splitting according to eq. S2, whereas the amount of Mn remaining at the electrode was quantified by XRF and normalized to the initial amount of Mn electrodeposited.

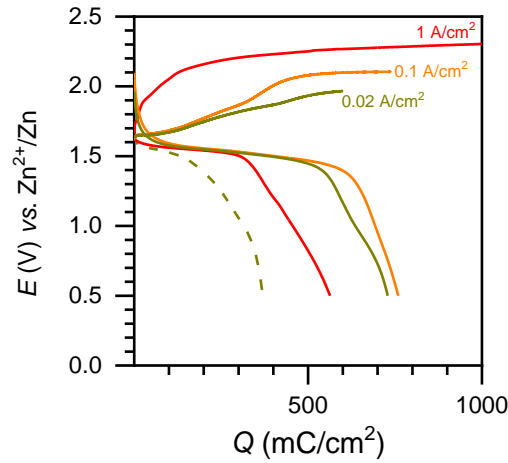


Fig. S12. First charge-discharge cycle recorded at spinel $\text{Mn}_3\text{O}_4@\text{CNF}$ electrodes in a 2 M acetate buffer (pH 4.7) for different charging rates and an identical discharge rate (-0.6 mA/cm^2). For comparison, the first discharge directly recorded at a pristine $\text{Mn}_3\text{O}_4@\text{CNF}$ electrode in the same buffer (*i.e.*, without passing through a first charging step) is overlaid (dashed line).

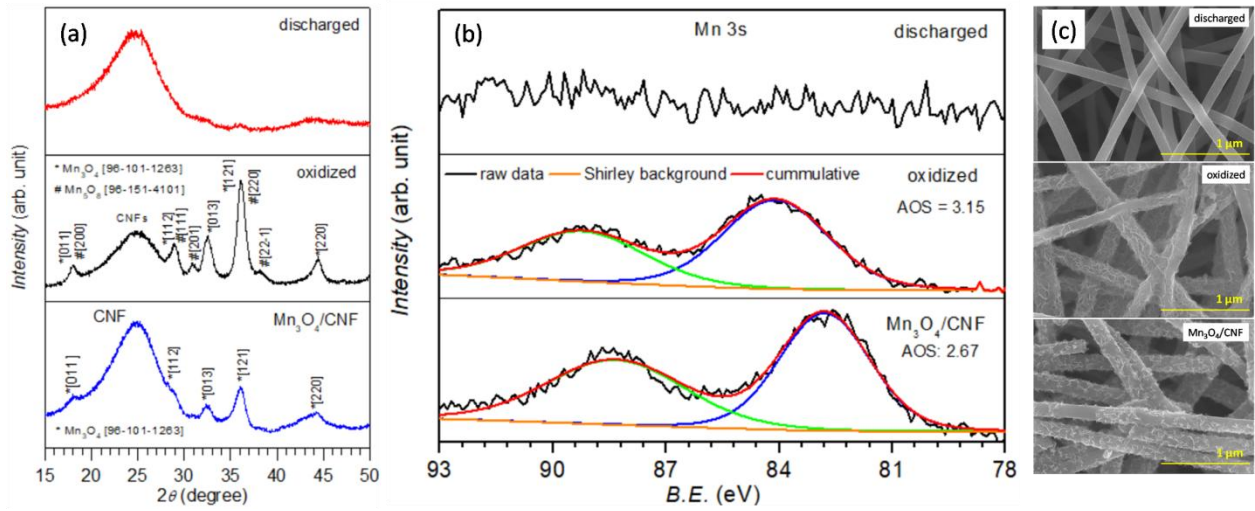


Fig. S13. Post-mortem (a) XRD, (b) core level Mn 3s XPS spectra, and (c) FEG-SEM images for $\text{Mn}_3\text{O}_4@\text{CNF}$ samples at three different stages: (bottom) pristine, (middle) oxidized at 0.02 mA/cm^2 , and (top) fully discharged at -0.6 mA/cm^2 after the oxidation step in a 2 M acetate buffer (pH 4.7) solution without Mn^{2+} .

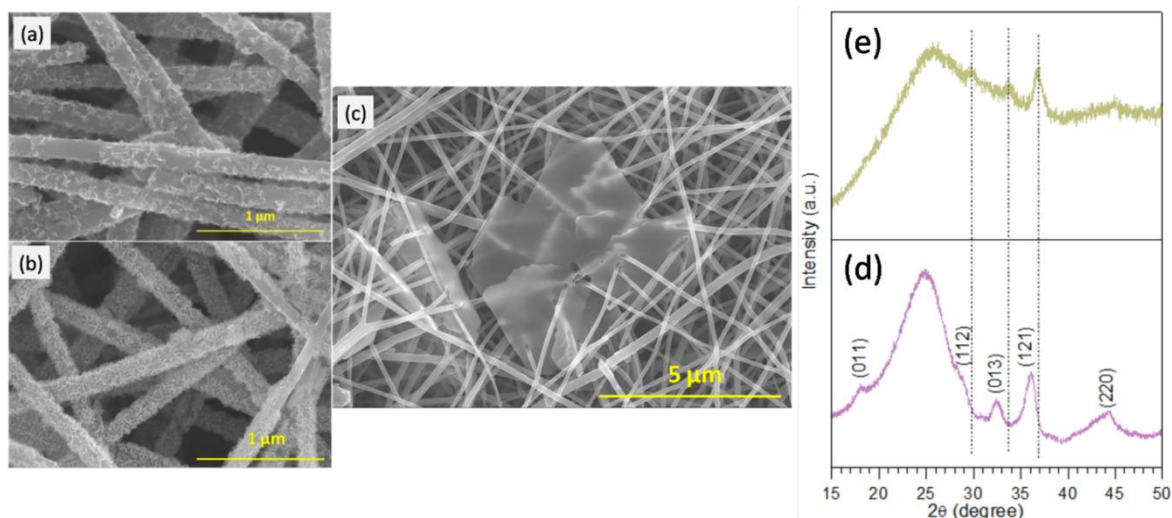


Fig. S14. FEG-SEM images of (a) a pristine $\text{Mn}_3\text{O}_4@\text{CNF}$ electrode, (b) a $\text{Mn}_3\text{O}_4@\text{CNF}$ electrode oxidized at 0.02 mA/cm^2 , and (c) the same electrode as in b but after a subsequent discharge at -0.6 mA/cm^2 in an unbuffered aqueous 1 M ZnSO_4 containing 0.3 M Mn^{2+} (pH 4.4). (d-e) XRD patterns of (bottom) the electrodes in a and (top) in b. The two weak signals appearing between $2\theta = 29\text{--}35^\circ$ are neither due to $\text{Mn}_3\text{O}_4/\text{amorphous MnO}_2$ nor due to Zn_yMnO_x structures, rather these are possibly due to residual ZnSO_4 electrolyte trapped into the electrode.^{S5}

Note on the Cyclability of Mn₃O₄@CNF in a mild buffered electrolyte

The faradaic discharge of the Mn₃O₄@CNF electrode proceeds according to a proton-coupled electrodisolution mechanism. Therefore, the only way to recharge the electrode is by back electrodeposition of a solid MnO_x from the solubilized Mn²⁺. Accordingly, Mn₃O₄@CNF electrodes were submitted to a galvanostatic discharge/charge (GDC) cycling in a 1.3 M Al(OTf)₃ or a 2 M acetate buffer electrolyte preloaded with 0.3 M Mn²⁺ (Fig. S15). The charge capacity was fixed to $Q_T = 1 \text{ C/cm}^2$. In both electrolytes, the charges were characterized by a well-defined plateau at 1.65 V (Fig. S15, note that in the absence of a Zn^{II} salt in the electrolyte, the charging process relies most likely on HER at the Zn anode, making it difficult to properly discuss the corresponding voltage value). FEG-SEM image of the charged electrode revealed the deposit of MnO_x coating over the CNFs, which according to the XRD and AOS of Mn in the XPS data has been identified as amorphous MnO₂ (Fig. S16). As expected, the cyclability of the Mn₃O₄@CNF electrodes in both electrolytes results from the Mn²⁺ present in large excess in the electrolyte, which upon electrochemical oxidation (charge) leads to the back deposition of an amorphous MnO₂ coating onto the CNFs. Accordingly, after a complete GDC cycle in the acetate buffer containing Mn²⁺, the Mn₃O₄ on the CNFs is no more available since it has been fully electrodisolved and replaced by an amorphous MnO₂ coating. This is a general mechanism that thus applied to any MnO_x@CNF electrodes, as attested by the XRD analysis of all fully recharged electrodes (see Fig. S5). Finally, up to 1400 GCD cycles could be achieved in the Al³⁺-based aqueous electrolyte containing Mn²⁺ (Fig. S15), with remarkably stable charge-discharge potentials, high *CEs* ($\geq 98.0\%$) and good energy efficiencies ($EE \geq 80\%$). These performances are close to those we have previously reported for amorphous MnO₂@CNF electrodes cycled in an Al³⁺-based electrolyte.^{S6} It is noted that the cyclability in the acetate buffered electrolyte is slightly lower (Fig. S15), with *CEs* $\geq 95.5\%$ over 50 cycles.

The crucial role of the Mn²⁺ additive to achieve a high cyclability of the cathode was confirmed by cycling the Mn₃O₄@CNF electrode in a 2 M acetate buffer of pH 4.7, initially free of Mn²⁺ (Fig. S15). While the first discharge leads to complete electrodisolution of the Mn₃O₄ coating and release of Mn²⁺ ions in the electrolyte, the subsequent charge now exhibits two well-defined plateaus (see Fig. S15). The first one is reminiscent of the back electrochemical oxidation of the just released Mn²⁺ ions into an amorphous deposit of MnO₂ on the CNFs, with negligible pH and [Mn²⁺] gradients at the electrode interface (similar to what we observed in Fig. S1). Its limited capacity indicates that only a fraction (*i.e.*, 60%) of the electrodisolved Mn²⁺ can be back electrodeposited because of mass transport limitation

in the bulk electrolyte.^{S4} Thereafter, the sharp increase in potential marks the concentration polarization ensuing from Mn^{2+} depletion close to the electrode. The second plateau at high voltage is likely the consequence of the oxygen evolution reaction (OER). This irreversible faradaic process contributes to a poor *CE* of 80% for the first cycle (compared to 98% for the same electrode cycled in the electrolyte containing 0.3 M Mn^{2+} additive (Fig. S15). Then, the electrode capacity rapidly fades upon continuous cycling because of the steady loss of Mn^{2+} by diffusion far into the “bulk” of the electrolyte. The above results, therefore, emphasize that the pre-addition of Mn^{2+} serves as a reservoir to facilitate the back re-electrodeposition of amorphous MnO_2 promoting thus the cycling of the cell.

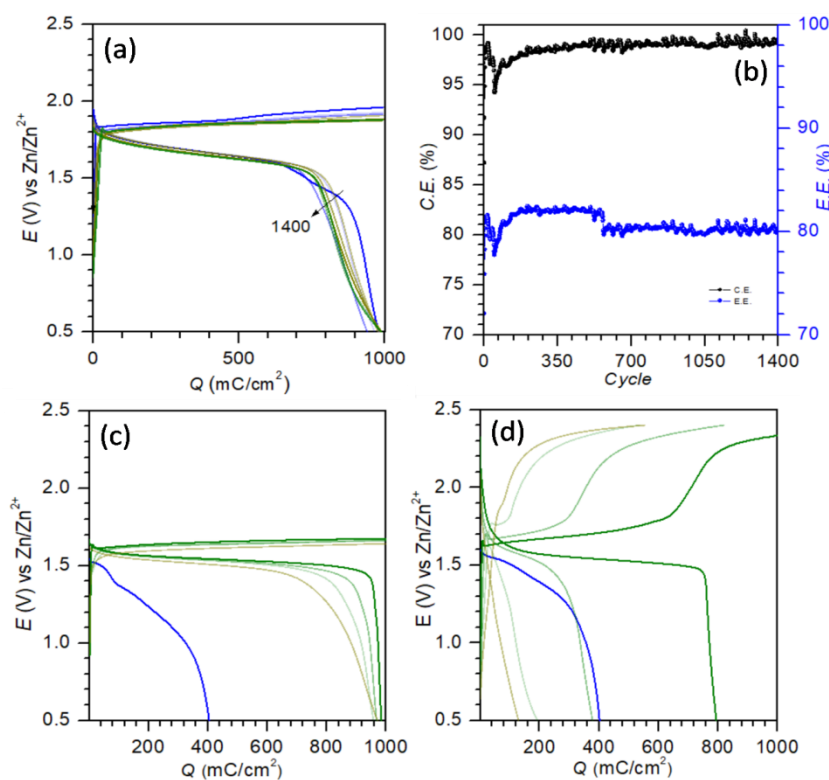


Fig. S15. (a) (blue → dark yellow → olive) Long-term galvanostatic charge-discharge cycling of a $\text{Mn}_3\text{O}_4@\text{CNF}$ electrode (only some specific cycles are shown over 1400) in a 1.3 m $\text{Al}(\text{OTf})_3$ electrolyte containing 0.3 M Mn^{2+} (pH 1.7) and (b) the corresponding (black) CE and (blue) EE values. (c) (blue) First discharge at $-0.6 \text{ mA}/\text{cm}^2$ and (olive → dark yellow) subsequent galvanostatic charge-discharge cycles at $\pm 1 \text{ mA}/\text{cm}^2$ recorded at a $\text{Mn}_3\text{O}_4@\text{CNF}$ electrode (only the 2nd, 5th, 10th, and 50th cycles over 50 are shown) in a 2 M acetate buffer (pH 4.7) containing 0.3 M Mn^{2+} . (d) Same experiment as in c but initially without Mn^{2+} in the electrolyte.

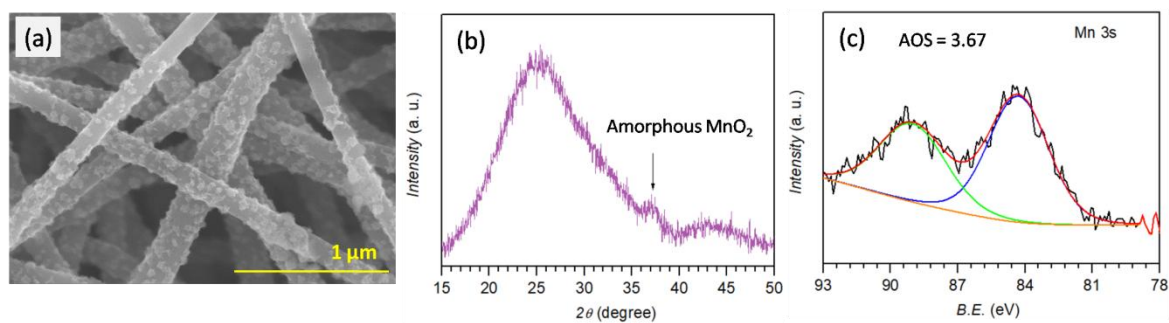


Fig. S16. (a) FEG–SEM image, (b) XRD pattern, and (c) core-level Mn 3s XPS spectra of electrodes after the first re-electrodeposition process in a 2 M acetate buffer containing 0.3 M Mn^{2+} (pH 4.7).

Supplementary Table

Table S1.^ΔElectrochemical data recently reported in various aqueous electrolytes for different low-valence MnO_x electrodes.

MnO _x structures	Aqueous Electrolytes [®]	Discharge capacity and cycle life	Charge storage Mechanism	Ref
Spinel Mn ₃ O ₄ (Hausmannite)	2 M ZnSO ₄ pH = n/a	239 mAh/g at 0.1 A/g <110 mAh/g at 0.5 A/g(300 cycles)	#(de)intercalation of Zn ²⁺ and H ⁺	S7
Spinel Mn ₃ O ₄	2 M ZnSO ₄ + 0.15 M MnSO ₄ pH = n/a	232 mAh/g at 0.4 A/g 1300 cycles, CE = 97%	#(de)intercalation of Zn ²⁺ and H ⁺	S8
Spinel Mn ₃ O ₄	2 M ZnSO ₄ + 0.1 M MnSO ₄ pH = n/a	212 mAh/g at 0.5 A/g 200 cycles, CE = 97%	#(de)intercalation of Zn ²⁺ and H ⁺	S9
Spinel Mn ₃ O ₄	2 M ZnSO ₄ + 0.1 M MnSO ₄ pH = n/a	<210 mAh/g at 0.5 A/g 500 cycles, CE = 100%	Zn ²⁺ and H ⁺ co-insertion	S10
Spinel Mn ₃ O ₄	2 M ZnSO ₄ + 0.1 M MnSO ₄ pH = n/a	514 mAh/g at 0.5 A/g 221 mAh/g at 3 A/g Capacity retention = 44%at 3 A/g, 600 cycles	#(de)intercalation of Zn ²⁺ and H ⁺	S11
Spinel Mn ₃ O ₄	2 M ZnSO ₄ + 0.1 M MnSO ₄ pH = 4.4	<150 mAh/g at 1 A/g, 700 cycles	(de)intercalation of Zn ²⁺ and H ⁺	S12
Spinel Mn ₃ O ₄	1 M ZnSO ₄ + 0.1 M MnSO ₄ + 1 M Na ₂ SO ₄ , pH = n/a	329 mAh/g at 1 A/g <120 mAh/g, 2000 cycles at rate = n/a	(de)intercalation of Zn ²⁺	S13
Spinel Mn ₃ O ₄	2 M ZnSO ₄ + 1 M MnSO ₄ pH = n/a	132 mAh/g at 0.5 A/g Capacity retention = 92%, 500 cycles	#(de)intercalation of H ⁺	S14
Spinel Mn ₃ O ₄	2 M ZnSO ₄ pH = n/a	<120 mAh/g at 0.1 A/g Capacity retention = 65%, 800 cycles	#(de)intercalation of Zn ²⁺ and H ⁺	S15
Spinel Mn ₃ O ₄	2 M ZnSO ₄ + 0.2 M MnSO ₄ pH = n/a	332 mAh/g at 0.1 A/g 149 mAh/g at 1 A/g Capacity retention = 92.5% at 1 A/g, 1500 cycles	#(de)intercalation of Zn ²⁺ and H ⁺	S16
Co-doped Mn ₃ O ₄ (Mn _{3-x} Co _x O ₄)	2 M ZnSO ₄ + 0.2 M MnSO ₄ pH = n/a	362 mAh/g at 0.2 A/g 250 cycles, CE = 81%	#(de)intercalation of Zn ²⁺ and H ⁺	S17
O _δ -Mn ₃ O ₄ (bulk oxygen defects)	2 M ZnSO ₄ + 0.2 M MnSO ₄ pH = n/a	88 mAh/g at 5 A/g Capacity retention = 95.7%, 12000 cycles	#(de)intercalation of Zn ²⁺ and H ⁺	S18
O _δ -MnO ₂ (bulk oxygen defects)	1 M ZnSO ₄ + 0.2 M MnSO ₄ pH = n/a	345 mAh/g at 0.2 A/g Capacity retention = 100%, 100 cycles	(de)intercalation of Zn ²⁺	S19

$\text{H}_{1.57}\text{Mn}_2\text{O}_4$	2 M ZnSO_4 + 0.1 M MnSO_4 pH = n/a	281 mAh/g at 0.1 A/g, Capacity retention = 95.5%, 100 cycles	(de)intercalation of Zn^{2+} and H^+	S20
$\text{Mn}^{2+,4+}\text{O}_x$ (MnO_x)	2 M ZnSO_4 + 0.1 M MnSO_4 pH = n/a	First discharge \approx 200 mAh/g at 0.5 A/g 305 mAh/g after 600 cycles	(de)intercalation of Zn^{2+}	S21
Cryptomelane-Type $\text{KMn}_8\text{O}_{16}$	1 M ZnSO_4 + 0.3 M K_2SO_4 + 0.05 M MnSO_4 pH = n/a	135 mAh/g at 0.1 A/g, Capacity retention = 55%, 100 cycles	$\#$ (de)intercalation of Zn^{2+}	S22
$\text{MnO}_2\text{H}_{0.16}(\text{H}_2\text{O})_{0.27}$	1 M ZnSO_4 + 0.2 M MnSO_4 pH = n/a	276 mAh/g at 0.31 A/g 163 mAh/g at 1.85 A/g Capacity retention = 80.5% at 1.85 A/g, 2000 cycles	(de)intercalation of Zn^{2+} and H^+	S23
Al-intercalated α - MnO_2	PVA- ZnSO_4 aqueous gel electrolyte	275 mAh/g at 2 A/g Capacity retention = 94.5% 2000 cycles	$\#$ (de)intercalation of Zn^{2+}	S24
α - Mn_2O_3	3 M ZnSO_4 + 0.2 M MnSO_4 pH = n/a	202 mAh/g at 0.2 A/g Capacity retention = 99% 120 cycles	$\#$ (de)intercalation of Zn^{2+}	S25
α - Mn_2O_3	2 M ZnSO_4 + 0.1 M MnSO_4 pH = n/a	<100 mAh/g at 2 A/g 2000 cycles	(de)intercalation of Zn^{2+}	S26
Mn_2O_3	2 M ZnSO_4 + 0.2 M MnSO_4 pH = n/a	164 mAh/g at 3.08 A/g Capacity retention = 89% 3000 cycles	$\#$ (de)intercalation of Zn^{2+} and H^+	S27
$\text{Al}_x\text{MnO}_2 \cdot n\text{H}_2\text{O}$	5 M $\text{Al}(\text{OTf})_3$ pH = n/a	467 mAh/g at 0.03 A/g Capacity retention = 58%, 60 cycles	(de)intercalation of Al^{3+}	S28
Spinel Mn_3O_4	1 M NH_4NO_3 pH = n/a	183 mAh/g at 0.1 A/g Capacity retention <50%, 200 cycles	(de)intercalation of NO_3^-	S29
$\text{K}_{0.27}\text{MnO}_2 \cdot 0.54\text{H}_2\text{O}$	2 M ZnSO_4 + 0.3 M MnSO_4 pH = 3.8	288 mAh/g at 0.1 A/g, Capacity retention = 92%, 300 cycles	(de)intercalation of H_3O^+	S30
$\text{Zn}_{0.2}\text{Mn}_3\text{O}_4$	20 M ZnCl_2 + 5 M NH_4Cl	<250 mAh/g at 0.05 A/g Capacity retention <70%, 90 cycles	(de)intercalation of Cl^-	S31
MnO_x	0.5 M $\text{CH}_3\text{COONH}_4$	176 mAh/g at 0.5 A/g \leq 120 mAh/g at 5 A/g 10000 cycles	(de)intercalation of NH_4^+	S32
Amorphous and crystalline MnO_x	Various unbuffered ³⁶ and buffered ⁵ aqueous electrolytes	After first discharge : 490 mAh/g_{MnO2} at 1.9 A/g_{MnO2}	\rightarrow First discharge $\text{MnO}_x \rightarrow \text{Mn}^{2+}(\text{aq})$	This work ³⁶

(1 < x ≤ 2) (e.g., Mn ₃ O ₄ , MnO ₂)		1400 cycles, CE ≥ 98% 1.3 m Al(OTf) ₃ + 0.3 M Mn ²⁺	→ after first discharge: Re-electrodeposited amorphous MnO ₂ ↔ Mn ²⁺ (aq)	
---	--	---	---	--

^AElectrochemical data for high valence MnO₂ structures (AOS ~ 4.0) is summarized in a recent report by Mateos *et al.*⁵⁴ from our group.

^Btypical ZHS precipitation in ZnSO₄ based electrolytes.

[#]structural changes during a few activation cycles and then insertion in the induced structures (e.g., Birnessite MnO₂.nH₂O).

[@]prepared by galvanostatic electrochemical transformation from spinel Mn₃O₄(Al³⁺ insertion).

[%]unbuffered electrolytes: 1 M ZnSO₄ (pH 4.7), 1 M NH₄Cl (pH 5.1), 1.3 m Al(OTf)₃ (pH 1.7), 1 M MnSO₄ (pH 7.0).

[§]2 M acetate buffer (pH 4.7).

[&]proton-coupled electrochemical reactions where a weak Brønsted acid (e.g., aqua [Al(H₂O)₆]³⁺, [Zn²(H₂O)₆]⁺, [Mn(H₂O)₆]²⁺, or NH⁴⁺ ions, and CH₃COOH) serves as a proton donor.

n/a: not specified.

References

- [S1] A. Singh, A. Rafie, V. Kalra, *Sustainable Energy Fuels* **2019**, *3*, 2788.
- [S2] A. Singh, O. Sel, H. Perrot, V. Balland, B. Limoges, C. Laberty-Robert, *J. Mater. Chem. A* **2021**, *9*, 1500.
- [S3] J. Liu, Y. Zhang, Q. Gu, A. Sheng, B. Zhang, *Minerals* **2020**, *10*, 690.
- [S4] M. Mateos, N. Makivic, Y.-S. Kim, B. Limoges, V. Balland, *Adv. Energy Mater.* **2020**, *10*, 2000332.
- [S5] A. C. Tizzoni, N. Corsaro, C. D'Ottavi, S. Licoccia, S. Sau, P. Tarquini, *Int. J. Hydrogen Energy* **2015**, *40*, 4065.
- [S6] V. Balland, M. Mateos, A. Singh, K. D. Harris, C. Laberty-Robert, B. Limoges, *Small* **2021**, *17*, 2101515.
- [S7] J. Hao, J. Mou, J. Zhang, L. Dong, W. Liu, C. Xu, F. Kang, *Electrochim. Acta* **2018**, *259*, 170.
- [S8] J. Long, Z. Yang, F. Yang, J. Cuan, J. Wu, *Electrochim. Acta* **2020**, *344*, 136155.
- [S9] H. Chen, W. Zhou, D. Zhu, Z. Liu, Z. Feng, J. Li, Y. Chen, *J. Alloys Compd.* **2020**, *813*, 151812.
- [S10] C. Zhu, G. Fang, J. Zhou, J. Guo, Z. Wang, C. Wang, J. Li, Y. Tang, S. Liang, *J. Mater. Chem. A* **2018**, *6*, 9677.
- [S11] L. Chen, Y. F. Yuan, P. F. Du, S. M. Yin, M. Zhu, S. Y. Guo, *Nanotechnology* **2021**, *32*, 405403.
- [S12] M. Sun, D. S. Li, Y. F. Wang, W. L. Liu, M. M. Ren, F. G. Kong, S. J. Wang, Y. Z. Guo, Y. M. Liu, *ChemElectroChem* **2019**, *6*, 2510.
- [S13] L. Ma, L. Li, Y. Liu, J. Zhu, T. Meng, H. Zhang, J. Jiang, C. M. Li, *Chem. Commun.* **2018**, *54*, 10835.
- [S14] L. Wang, X. Cao, L. Xu, J. Chen, J. Zheng, *ACS Sustainable Chem. Eng.* **2018**, *6*, 16055.
- [S15] I. Stoševski, A. Bonakdarpour, B. Fang, S. T. Voon, D. P. Wilkinson, *Int. J. Energy Res.* **2020**, *45*, 220.
- [S16] L. Jiang, F. Ye, Z. Wu, L. Zhang, Q. Liu, Z. Tang, L. Hu, *J. Mater. Chem. A* **2021**, *9*, 27380.
- [S17] J. Ji, H. Wan, B. Zhang, C. Wang, Y. Gan, Q. Tan, N. Wang, J. Yao, Z. Zheng, P. Liang, J. Zhang, H. Wang, L. Tao, Y. Wang, D. Chao, H. Wang, *Adv. Energy Mater.* **2020**, *11*, 2003203.
- [S18] Q. Tan, X. Li, B. Zhang, X. Chen, Y. Tian, H. Wan, L. Zhang, L. Miao, C. Wang, Y. Gan, J. Jiang, Y. Wang, H. Wang, *Adv. Energy Mater.* **2020**, *10*, 2001050.
- [S19] T. Xiong, Z. G. Yu, H. Wu, Y. Du, Q. Xie, J. Chen, Y. W. Zhang, S. J. Pennycook, W. S. V. Lee, J. Xue, *Adv. Energy Mater.* **2019**, *9*, 1803815.
- [S20] Y. Wu, K. Zhang, S. Chen, Y. Liu, Y. Tao, X. Zhang, Y. Ding, S. Dai, *ACS Appl. Energy Mater.* **2019**, *3*, 319.
- [S21] Y. Fu, Q. Wei, G. Zhang, X. Wang, J. Zhang, Y. Hu, D. Wang, L. Zuin, T. Zhou, Y. Wu, S. Sun, *Adv. Energy Mater.* **2018**, *8*, 1801445.
- [S22] J. Cui, X. Wu, S. Yang, C. Li, F. Tang, J. Chen, Y. Chen, Y. Xiang, X. Wu, Z. He, *Front. Chem.* **2018**, *6*, 352.
- [S23] Q. Zhao, X. Chen, Z. Wang, L. Yang, R. Qin, J. Yang, Y. Song, S. Ding, M. Weng, W. Huang, J. Liu, W. Zhao, G. Qian, K. Yang, Y. Cui, H. Chen, F. Pan, *Small* **2019**, *15*, 1904545.
- [S24] C. Chen, M. Shi, Y. Zhao, C. Yang, L. Zhao, C. Yan, *Chem. Eng. J.* **2021**, *422*, 130375.
- [S25] Y. Ma, Y. Ma, T. Diemant, K. Cao, X. Liu, U. Kaiser, R. J. Behm, A. Varzi, S. Passerini, *Adv. Energy Mater.* **2021**, *11*, 2100962.
- [S26] B. Jiang, C. Xu, C. Wu, L. Dong, J. Li, F. Kang, *Electrochim. Acta* **2017**, *229*, 422.

- [S27] D. Feng, T. N. Gao, L. Zhang, B. Guo, S. Song, Z. A. Qiao, S. Dai, *Nanomicro Lett.* **2019**, *12*, 14.
- [S28] C. Wu, S. Gu, Q. Zhang, Y. Bai, M. Li, Y. Yuan, H. Wang, X. Liu, Y. Yuan, N. Zhu, F. Wu, H. Li, L. Gu, J. Lu, *Nat. Commun.* **2019**, *10*, 73.
- [S29] H. Jiang, Z. Wei, L. Ma, Y. Yuan, J. J. Hong, X. Wu, D. P. Leonard, J. Holoubek, J. J. Razink, W. F. Stickle, F. Du, T. Wu, J. Lu, X. Ji, *Angew. Chem. Int. Ed. Engl.* **2019**, *58*, 5286.
- [S30] L. Liu, Y. C. Wu, L. Huang, K. Liu, B. Duployer, P. Rozier, P. L. Taberna, P. Simon, *Adv. Energy Mater.* **2021**, *11*, 2101287.
- [S31] H. Jiang, X. Ji, *Carbon Energy* **2020**, *2*, 437.
- [S32] Y. Song, Q. Pan, H. Lv, D. Yang, Z. Qin, M. Y. Zhang, X. Sun, X. X. Liu, *Angew. Chem. Int. Ed. Engl.* **2021**, *60*, 5718.